ARTICLE

E-cadherin interacts with EGFR resulting in hyper-activation of ERK in multiple models of breast cancer

Gabriella C. Russo[1,2], Ashleigh J. Crawford[1,2], David Clark[3], Julie Cui[1], Ryan Carney[4], Michelle N. Karl[1,2], Boyang Su[5], Bartholomew Starich[1,2], Tung-Shing Lih[3], Pratik Kamat[1,2], Qiming Zhang[1], Praful R. Nair[1,2], Pei-Hsun Wu [1,2], Meng-Horng Lee[1], Hon S. Leong[5,6], Hui Zhang[3], Vito W. Rebecca[7] and Denis Wirtz [1,2✉]

The loss of intercellular adhesion molecule E-cadherin is a hallmark of the epithelial-mesenchymal transition (EMT), during which tumor cells transition into an invasive phenotype. Accordingly, E-cadherin has long been considered a tumor suppressor gene; however, E-cadherin expression is paradoxically correlated with breast cancer survival rates. Using novel multi-compartment organoids and multiple in vivo models, we show that E-cadherin promotes a hyper-proliferative phenotype in breast cancer cells via interaction with the transmembrane receptor EGFR. The E-cad and EGFR interaction results in activation of the MEK/ERK signaling pathway, leading to a significant increase in proliferation via activation of transcription factors, including *c-Fos*. Pharmacological inhibition of MEK activity in E-cadherin positive breast cancer significantly decreases both tumor growth and macro-metastasis in vivo. This work provides evidence for a novel role of E-cadherin in breast tumor progression and identifies a new target to treat hyper-proliferative E-cadherin-positive breast tumors, thus providing the foundation to utilize E-cadherin as a biomarker for specific therapeutic success.

INTRODUCTION

E-cadherin (E-cad), a transmembrane molecule ubiquitously expressed in normal epithelial tissues, promotes and maintains intercellular adhesion. Through interactions with β-catenin, E-cad becomes functional, resulting in the formation of adherens junctions between E-cad molecules on neighboring cells [1–5]. In the context of cancer, the loss of E-cad expression and gain of N-cadherin expression are associated with onset of invasion via the epithelial-to-mesenchymal transition (EMT) [1, 2]. EMT consists of a highly orchestrated cascade of molecular events, in which epithelial cells transition from a polarized, stationary state to an invasive, migratory morphology that is accompanied by a mesenchymal phenotype [2, 3]. These processes are believed to then trigger metastasis in carcinomas, i.e., cancers of epithelial origin. Together these results have long suggested that E-cad is a tumor suppressor gene and that its expression correlates with a better survival outcome in patients [2, 3]. However, considering that 80% of the most common type of breast cancer, invasive ductal carcinoma (IDC), are E-cad positive and can retain E-cad expression when metastasizing, the classification of E-cad as a tumor suppressor gene is being re-assessed [6–10]. This unanticipated association between poor clinical outcome and E-cad expression has prompted re-evaluation of its role in EMT and metastatic disease [7–9, 11]. Here, we provide evidence that E-cad plays an influential role in proliferation with mechanistic proof and clinical correlations.

Clinical data indicate that high E-cad expression in patients with IDC is associated with a worse overall survival rate in the Metabric database, and the expression of *CDH1* (gene that encodes E-cad) is correlated with both proliferation and metastatic gene sets in the TCGA invasive breast cancer RNA-seq database [7, 11]. These correlations suggest that E-cad may function as an oncogene in breast cancer rather than a tumor suppressor gene. Recent studies aimed at re-assessing E-cad function in cancer have focused on the role of E-cad in EMT and the cancer cell phenotypes related to metastatic potential and migration potential [8–10, 12]. Whether and how E-cad expression impacts proliferation in cancer cells is not well understood and the functional implications of E-cad interactions with other transmembrane proteins, such as EGFR, have yet to be fully elucidated [13–20].

As mentioned previously, E-cad is known to interact closely with dual-functioning β-catenin at the cell membrane, which forms a complex with α-catenin before binding with the cytoplasmic tail of E-cad [21, 22]. Once activated, E-cad links to the actin cytoskeleton and can form adherens junctions between neighboring cells. When it does not interact with E-cad, β-catenin can also function as a transcription factor in the nucleus where it can impact cell growth [21, 22]. There is some evidence of E-cad interactions with RTKs, including EGFR [13, 20, 23]. Whether E-cad/EGFR interactions occur in cancer cells and the impact of such interactions on tumor progression, including cancer cell proliferation, remains largely

[1]Department of Chemical and Biomolecular Engineering, Johns Hopkins University, 3400 N Charles St, Baltimore, MD 21218, USA. [2]Johns Hopkins Physical Sciences–Oncology Center and Institute for NanoBioTechnology, Johns Hopkins University, 3400 N Charles St, Baltimore, MD 21218, USA. [3]Department of Pathology, The Johns Hopkins University School of Medicine, Baltimore, MD 21231, USA. [4]Department of Biophysics, Johns Hopkins University, 3400 N Charles St, Baltimore, MD 21218, USA. [5]Department of Medical Biophysics, University of Toronto, Toronto, ON, Canada. [6]Biological Sciences Platform, Sunnybrook Research Institute, Toronto, ON, Canada. [7]Department of Biochemistry and Molecular Biology, Johns Hopkins University School of Public Health, Baltimore, MD 21231, USA. ✉email: wirtz@jhu.edu

unexplored [13–15, 18–20]. Thus, it is vital to examine the potential role of E-cad in breast cancer cell proliferation to further unravel the disparity between clinical data and our molecular understanding of how E-cad functions in cancer.

Here, utilizing newly developed multi-compartment organoids and multiple in vivo models, we studied the impact of E-cad expression on breast cancer cell proliferation at both the primary and secondary metastatic sites [24, 25]. Remarkably, E-cad expression in breast cancer cells leads to upregulation of the ERK cascade within the greater MAPK signaling pathway in our tumor organoid model and in vivo studies in mice. E-cad interacts with EGFR at the cell surface, which leads to downstream hyper-activation of ERK. This E-cad–induced upregulation of the ERK cascade results in a dramatic increase in cancer cell proliferation, tumor growth, and metastatic outgrowth in vivo. When the phosphorylation of ERK is blocked by employing a highly specific MEK1/2 inhibitor [26], this hyper-proliferative effect is reversed. The TCGA invasive breast carcinoma (BRCA) RNA-seq dataset corroborates our elucidated mechanism and shows that E-cad (CDH1 expression) is positively correlated with various MAPK signaling gene sets. In sum, this work suggests that E-cad plays a pro-tumorigenic role and reveals new molecular targets for the treatment of patients with E-cad positive IDC tumors.

RESULTS

E-cad expression promotes proliferation in breast cancer cells

We first evaluated the clinical outcomes of patients with invasive ductal carcinoma (IDC), which often express high levels of E-cadherin (E-cad) utilizing the Metabric dataset [11]. This analysis revealed that high E-cad expression is associated with a worse overall survival (Fig. 1a). In addition to worse overall survival in the IDC subset of breast cancer (Fig. 1a), CDH1 (E-cad) expression is also correlated with increased metastasis and worse prognosis in the TCGA invasive breast cancer (BRCA) dataset (Extended Data Fig. 1a, Table 1). CDH1 expression was positively correlated with three breast cancer metastasis gene sets (Table 1), including one associated with poor prognosis. Additionally, CDH1 expression was also anti-correlated with genes downregulated during lymphatic invasion (Table 1).

We sought to explore how else E-cad impacts cancer progression and probed the TCGA invasive breast carcinoma dataset for correlations with proliferation related genes. Our analysis showed that CDH1 expression is correlated with several proliferation and cell-cycle based gene sets (Extended Data Fig. 1b, Table 2). CDH1 expression is also anti-correlated with genes involved in the proliferation-arrest inducing p53 pathways, further hinting that CDH1 expression promotes proliferation. Based on this analysis, we hypothesized that E-cad (CDH1) promotes breast cancer metastasis by promoting cancer cell proliferation.

To mechanistically test this hypothesis, we first performed direct comparisons of paired cancer cells with high and low E-cad expression through use of genetically engineered cell lines created from the same parental cells. We determined the endogenous expression level of E-cad in seven commonly used ductal carcinoma breast cancer cell lines, spanning all hormone receptor subtypes- HR+, HER2+, and TNBC (Extended Data Fig. 1c) [26]. Of these, we chose three cell lines classified as IDC that were suitable for in vivo modeling. MCF7 and MDA-MB-468 endogenously express E-cad (denoted E-cad+), while MDA-MB-231, known for its high proliferative index and metastatic potential in vivo, does not endogenously express E-cad (denoted E-cad−) [27, 28]. We generated E-cad shRNA lentiviral knockdowns for MDA-MB-468 and MCF7 cells (denoted E-cad KD) and an E-cad lentiviral knock-in for MDA-MB-231 cells (denoted E-cad KI). After these modifications, we confirmed changes in E-cad expression

via western blots (Fig. 1b). We also confirmed expected functional changes associated with E-cad by assessing the impact of E-cad manipulations on β-catenin localization within the cells. β-catenin links the cytoplasmic domain of E-cad to the actin filament network, allowing E-cad to function as a cell-cell adhesion molecule [1]. Immunofluorescence microscopy revealed β-catenin accumulation in the nucleus in E-cad− cells, as anticipated, and localization in the cytoplasm and at the cell membrane in E-cad+ cells, where β-catenin can function in conjunction with E-cad (Fig. 1c) [1]. As expected, we also observed organized actin filaments in E-cad+ cells and a disorganized, wavy appearance in E-cad− cells (Fig. 1c) [1, 4].

We then compared the proliferation of these cell pairs in standard culture conditions (i.e. monolayer) and observed a significantly higher proliferation rate of E-cad+ cells compared to E-cad− cells (Extended Data Fig. 1d). However, this 2D environment is far from the 3D nature of a tumor and cells are artificially apically polarized. Hence, we recently developed a 3D multi-compartment tumor organoid system that mimics the primary breast tumor microenvironment, allowing us to study the impact of E-cad on cancer cell proliferation in a physiologically relevant model [24]. The core of these organoids contains a controlled number of cancer cells suspended in Matrigel, which is then encapsulated in a collagen I matrix, resulting in a collagen corona around the Matrigel core containing the cancer cells. This model mimics the basement membrane and the surrounding collagen-rich stroma of solid breast tumors (Fig. 1d) and allows us to monitor the proliferation and invasion of cancer cells from the core into the collagen layer under light microscopy.

We measured proliferation in this organoid model using the PrestoBlue viability assay and observed a significant increase in growth in E-cad+ organoids compared to Ecad- organoids (Fig. 1e) [29]. We confirmed a linear relationship between RFU and cell number to ensure these results correlated with increasing cell numbers (Extended Data Fig. 1e, f). We also tracked organoid progression under DIC light microscopy and observed expected migratory and invasive phenotype changes when E-cad expression was manipulated, i.e. single-cell migration compared to collective cell invasion (Extended Data Fig. 1g) [1–4]. After 5 days of growth, we conducted immunofluorescence staining on fixed organoids for proliferation marker Ki67 (red) and apoptosis marker cleaved caspase-3 (green) (Fig. 1f). We observed areas of highly proliferative Ki67+ cells in E-cad+ organoids accompanied by some apoptosis in the core and immediate invasive layer, where cancer cells were densely packed (Fig. 1f). These proliferative cells extended to the leading edge of the invasive cell front in E-cad+ organoids. We did not observe any Ki67+ cells in E-cad− organoids at this timepoint but observed positive cleaved-caspase 3 cells in the core of the E-cad− organoids (Extended Data Fig. 1h). These results confirm our previous observations: E-cad expression correlates with increased proliferation in breast cancer cells.

E-cad expression results in hyper-activation of ERK

To understand how E-cad promotes proliferation in cancer cells, we performed RT-qPCR analysis of genes associated with proliferation/growth pathways. The proliferation related MAPK pathway and the WNT pathway (related to E-cad function) [30, 31] showed the greatest change in E-cad+ versus E-cad− cancer cells (Fig. 2a and Extended Data Fig. 2a). The MAPK pathway is a three-tiered kinase cascade consisting of three main complexes: ERK, JNK, and p38. The ERK complex is of particular interest, as once activated, it can regulate processes such as proliferation, differentiation, and survival [30]. B-catenin is the central molecule of the WNT signaling pathway, playing roles as both a membrane-bound protein when activating E-cad and as a transcription factor when localized to the nucleus, where it can impact and regulate the cell cycle [31]. Our results showed that 30% of key genes in the
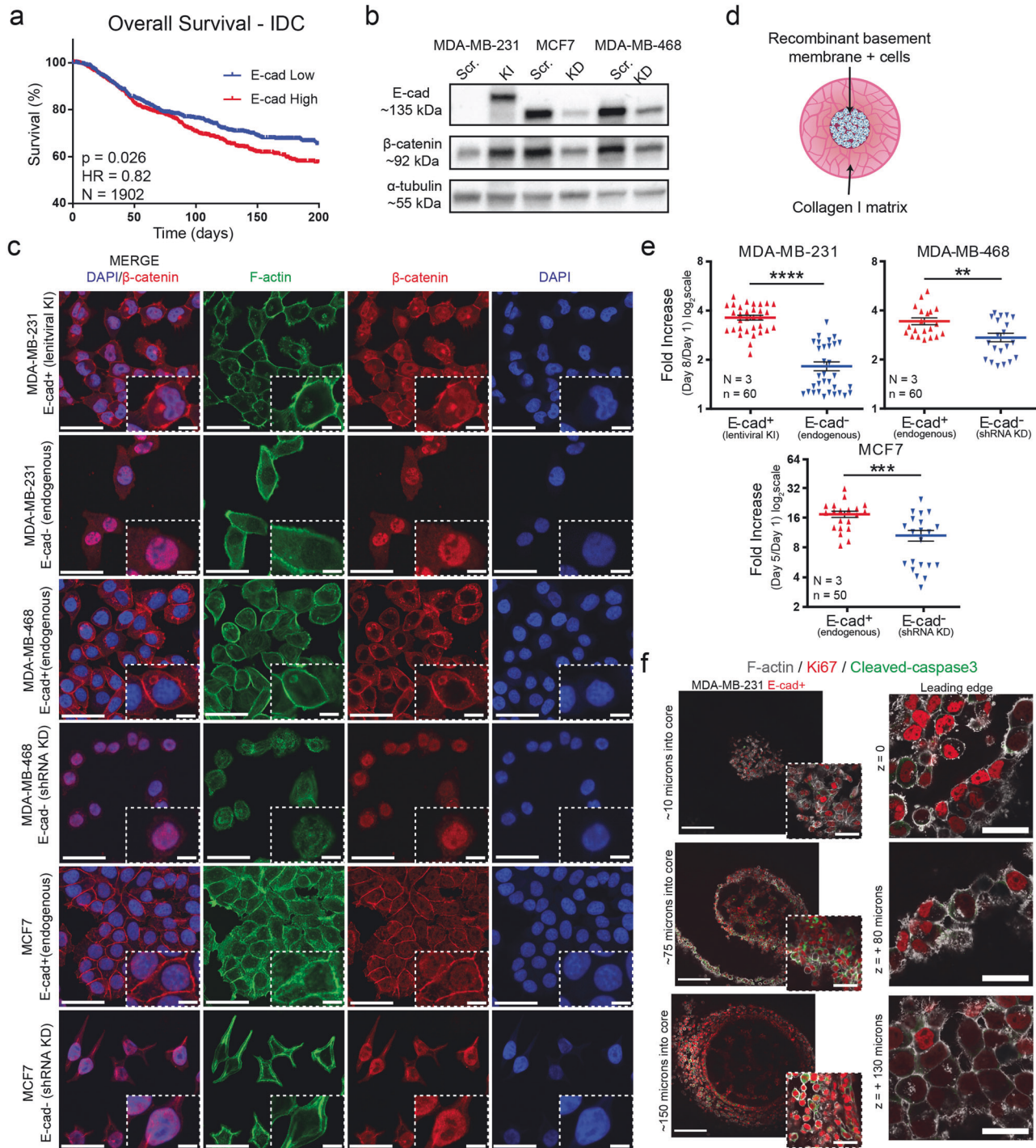
Fig. 1 Manipulation of E-cadherin expression impacts proliferation in breast cancer cells. a Survival plot based on Metabric dataset [11]. Low E-cad expression is defined here as 50 percentile or lower, while high E-cad expression is 50 percentile or higher. Sample size: $N = 1902$ patients. **b** Western blot assessment of E-cadherin, β-catenin, and a-tubulin (loading control) protein expression in E-cadherin shRNA-based knockdown (KD) or lentiviral knock-in (KI) and scramble controls (Scr.) for MDA-MB-231, MCF7, and MDA-MB-468 human breast cancer cells. **c** Immunofluorescence micrographs showing E-cad functional status via β-catenin localization in control and E-cad modified MDA-MB-231, MDA-MB-468, MCF7 cells in vitro. β-catenin is in red, F-actin is green, and nuclear DNA (DAPI) is blue. Scale bars = 50 μm and inset = 10 μm. $N = 3$. **d** Schematic of the 3D organoid system composed of Matrigel in the inner core and collagen I outer layer. **e** PrestoBlue fold increase of MDA-MB-231 ($n = 60$) ****$P \leq 0.0001$, MDA-MB-468 ($n = 60$) **$P = 0.0073$, and MCF7 ($n = 50$) ***$P = 0.0008$ comparing organoids on day 1 to day 8 or day 1 to day 5. $N = 3$ biological repeats for all cell lines. All data are mean ± SEM. Statistical test used: Mann–Whitney test, two sided for organoids. **f** Ki67 and cleaved-caspase 3 staining of MDA-MB-231 E-cad+ organoids on day 5 of culture. Scale bars: 200 μm, inset 50 μm and "leading edge" images scale bars: 50 μm. $N = 1$.

Table 1. TCGA invasive breast cancer (BRCA) - metastasis and prognosis-related gene sets correlation with CDH1 expression (Enrichment plots in Extended Data Fig. 1).

TCGA-BRCA dataset			
GSEA gene set	**Brief description**	**p-value for CDH1 expression being positively correlated with gene set signaling**	**p-value for CDH1 expression being anti-correlated with gene set signaling**
VANTVEER_BREAST_CANCER_POOR_PROGNOSIS	The optimal set of 70 prognostic markers predicting poor breast cancer clinical outcome (defined as developing metastases within 5 years).	0.013	1
PEDERSEN_METASTASIS_BY_ERBB2_ISOFORM_7	Genes linked with metastasis in breast cancer cells by expression of ERBB2.	2.24E-07	1
WANG_METASTASIS_OF_BREAST_CANCER_ESR1_UP	Genes whose expression in ER+ breast tumors positively correlates with developing distant metastases.	6.96E-06	1
CLASPER_LYMPHATIC_VESSELS_DURING_METASTASIS_DN	Selected genes downregulated during invasion of lymphatic vessels during metastasis.	1	5.43E-05

Table 2. TCGA invasive breast cancer (BRCA) – proliferation gene sets correlation with *CDH1* expression (Enrichment plots in Extended Data Fig. 1).

TCGA-BRCA dataset			
GSEA gene set	**Brief description**	**p-value for CDH1 expression being positively correlated with gene set signaling**	**p-value for CDH1 expression being anti-correlated with gene set signaling**
KEGG_CELL_CYCLE	Genes involved in regulating the cell cycle.	2.08E-09	1
HALLMARK_E2F_TARGETS	Genes encoding cell cycle related targets of E2F transcription factors.	5.00E-29	1
HALLMARK_G2M_CHECKPOINT	Genes involved in regulating the G2/M checkpoint of the cell cycle.	5.00E-29	1
HALLMARK_MITOTIC_SPINDLE	Genes important for mitotic spindle assembly.	4.82E-13	1
HALLMARK_P53_PATHWAY	Genes involved in p53 pathways and networks.	1	0.013

MAPK pathway were expressed at least 2-fold higher in E-cad+ cells compared to E-cad− breast cancer cells (Fig. 2a and Extended Fig. 2a). Upregulated genes in the ERK cascade included *MAP2K1 & MAP2K2* (which encode MEK1/2), *MAPK3 & MAPK1* (which encode ERK1/2), and downstream transcription factor *FOS*. In the WNT signaling pathway, approximately 27% of genes were expressed at least 2-fold higher when E-cad was present (Fig. 2a). In addition to the upregulation of β-catenin (*CTNNB1*), we observed upregulation of *GSK3β* (Fig. 2a), which can degrade β-catenin through interactions with *APC* and *AXIN1* [31]. Genes downstream of *CTNNB1*, including Lymphoid Enhancer Binding Factor 1 (*LEF1*) and Cyclin D1 (*CCND1*) were concurrently upregulated.

To assess the functional consequences of MAPK and WNT pathway activation, we treated the tumor organoids with nine small-molecule inhibitors that targeted key molecules of these pathways, such as the MAPK members ERK, MAPK8/9, c-Jun, p38, and B-Raf as well as the WNT signaling proteins β-catenin, AKT, PKC, and GSK3β (Table 3). We quantified the resulting volume change for each compartment over the course of the experiment, as assessing the inner core volume change from day 1 to day 7 is analogous to using the PrestoBlue viability assay to calculate fold

increase for this organoid model (Fig. 2b, Extended Data Fig. 2b) [29]. Change in volume of the outer collagen layer capture if cells are actively degrade and re-organize the matrix. Inhibition of JNK via SP600125, ERK via PD0325901, and GSK3β via CHIR-98014 significantly slowed the growth of organoid inner volume (Fig. 2c, Table 3). We also observed the application of these inhibitors resulted in fewer cells in the outer collagen layer, leading to smaller volume change over the duration of the experiment (Extended Data Fig. 2c).

The small-molecule inhibitor screening was also reflective of what was observed at the mRNA level in our PCR data. The JNK inhibitor SP600125 directly targets the genes encoded by *MAPK8* and *MAPK9*, which are upregulated by E-cad expression (Fig. 2a and Extended Data Fig. 2a). Accordingly, JNK inhibitor SP600125 successfully slowed tumor organoid progression. Another JNK inhibitor BI-7893 (which targets c-Jun) had little impact on progression as E-cad expression caused no change in *JUN* (the gene that encodes c-Jun) expression (Fig. 2c). Thus, the coupling of these datasets could potentially allow us to narrow down the mechanism by which E-cad is promoting hyper-proliferation.

We further explored the ERK cascade in the MAPK pathway by studying the impact of MEK inhibition using highly selective MEK
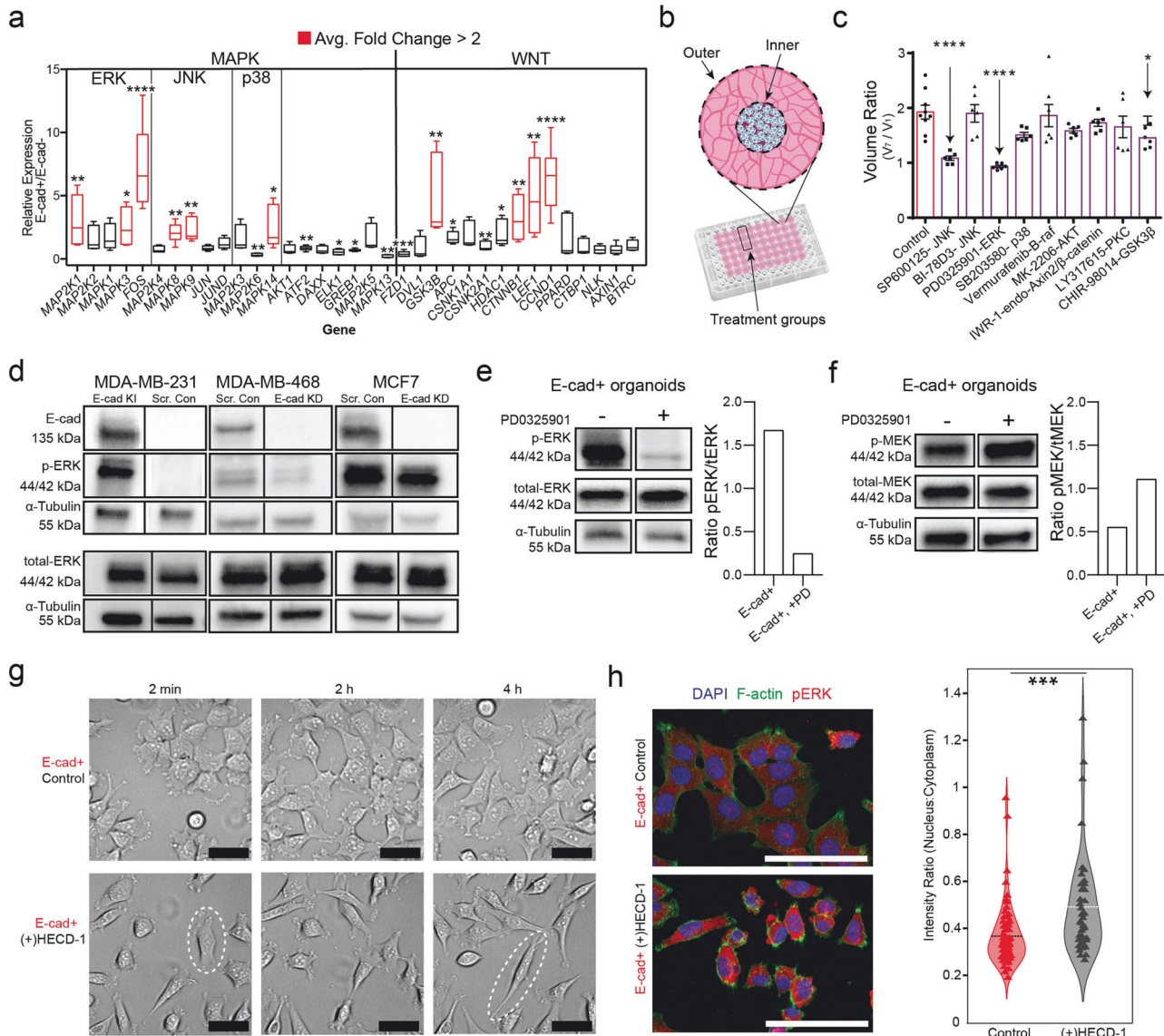
Fig. 2 E-cadherin promotes hyper-proliferation via the MAPK pathway. a Box plots: relative expression of key genes in the MAPK and WNT signaling pathways MDA-MB-231 E-cad+ to MDA-MB-231 E-cad− organoids assessed via RT-qPCR. Fold change of ±2 is considered biologically relevant. $N = 3$ biological repeats. P-values calculated via T.Test (2 tailed, equal variance), from left to right: $**P = 0.009$, $*P = 0.013$, $****P = 1.880E-05$, $**P = 0.002$, $**P = 0.002$, $***P = 0.0003$, $*P = 0.02$, $**P = 0.006$, $*P = 0.03$, $*P = 0.03$, $**P = 0.006$, $***P = 0.0003$, $**P = 0.002$, $*P = 0.1$, $**P = 0.00995$, $*P = 0.02$, $**P = 0.002$, $**P = 0.004$, $****P = 1.62E-06$. **b** Schematic of high-throughput experiment to assess response to inhibitors listed in Table 3 and schematic of volume measurements used to calculate inner and outer volume ratios. **c** Inner volume ratio of 10 μM inhibitor screening ($N = 1$, $n = 5–6$ per condition) ANOVA used to calculate P-values. **d** Representative western blot results, confirming higher levels of p-ERK in E-cad+ organoids for all cell line pairs. **e** Western blot images and quantification of MDA-MB-231 E-cad+ organoids treated with MEK inhibitor PD0325901, resulting in decrease in p-ERK expression. **f** Western blots images and quantification of MDA-MB-231 organoids treated with PD0325901, resulting in a slight increase in p-MEK expression. **g** Phase contrast microscopy images of MDA-MB-231 E-cad+ during $t = 2$ min, 2 h, and 4 h of migration study to test impact of an E-cad functional blocking antibody. Scale bars = 50 μm. **h** Immunofluorescence staining of phosphorylated ERK (red), shown with nuclear stain (blue) and F-actin stain (green). Scale bars = 50 μm. Ratio of nuclear expression to cytoplasmic expression of phospho-ERK increases in response to HECD-1 treatment, indicating more phospho-ERK is localizing to the nucleus. $N = 3$ biological repeats, $n = 4$ technical repeats.

inhibitor PD0325901 (Mirdametinib), as it was the most effective at stopping E-cad-mediated tumor organoid growth (Fig. 2a, c). PD0325901 is a small-molecule inhibitor that prevents ERK activation by targeting MEK1/2 kinase activity, which activates ERK by phosphorylating sites Y204 and Y187 [30, 32]. Selective and well characterized small-molecule inhibitors were chosen because shRNA knockdown of MEK or ERK would be fatal to the cells [33], and we wanted to assess the potential for targeting this pathway in pre-clinical models of breast cancer [33]. Results showed that PD0325901 was effective at reducing proliferation at a dose as low

as 1 μM (Extended Data Fig. 2d). E-cad+ organoids featured increased levels of phosphorylated ERK (phospho-ERK) at sites Y187 and Y204 compared to E-cad− organoids in all tested cell pairs (Fig. 2d). We also observed a 3.5-fold increase in the IC_{50} value when E-cad was expressed, indicating that more MEK inhibitor was required when E-cad was present to achieve the same decrease in cell growth (Extended Data Fig. 2e). We confirmed this result using the more potent but less specific MEK1/2 inhibitor Trametinib (Extended Data Fig. 2e) [34, 35]. We observed that MEK1/2 inhibition resulted in a large decrease in

Table 3. List of inhibitors in functional assessment of MAPK and WNT pathways in organoid model.

Inhibitor	Target
SP600125	JNK
BI-78D3	JNK
PD0325901	ERK
SB203580	p38
Vemurafenib	B-Raf
MK-2206	AKT
IWR-1-endo	Axin2/β-catenin
LY317615	PKC
CHIR-98014	GSK3β

phospho-ERK levels but slightly increased MEK phosphorylation in both E-cad+ and E-cad− organoids (Fig. 2e, f and Extended Data Fig. 2f, g). Together these results suggest that E-cad expression induces a hyper-proliferative phenotype in breast cancer cells through ERK activation.

Next, we sought to understand if this activation of ERK relied on the well-known mechanical role of E-cad: promoting cell-cell adhesion [5]. We treated E-cad+ cancer cells with the functional blocking antibody HECD-1 to prevent formation of intercellular adherens junctions [36]. We first confirmed that the functional blocking antibody prevented cell-cell adhesion in E-cad+ cells via live cell microscopy over the incubation period: cells became more mesenchymal in morphology, i.e. more elongated, less cobble stone like in morphology, similar to MDA-MB-231 E-cad− cells' morphology (Fig. 2g, Extended Data Fig. 2h). In HECD-1-treated cells, actin filament organization was lost due to the disruption of activated E-cad linking to the actin cytoskeleton, confirming the anticipated phenotypic changes when treating with an E-cad functional blocking antibody (Extended Data Fig. 2i) [1, 4]. Intriguingly, analysis of phospho-ERK intensity measured via immunofluorescence revealed a shift from the cytoplasm to the nucleus after treatment with HECD-1 (Fig. 2h). We also observed a decrease in the areas of the nucleus and the cytoplasm of HECD-1-treated cells, likely due to the changes in cell morphology with nuclear size changes being expected when cell shape becomes dynamic (Extended Data Fig. 2j). The increase in nuclear phospho-ERK intensity suggests the cells are no longer producing phospho-ERK in the cytoplasm, thus indicating E-cad function is essential for continued activation of ERK prior to translocation into the nucleus. This localization shift of phospho-ERK into the nucleus, where it can influence proliferation, further supports our hypothesis that increased ERK activation is causing the hyper-proliferative phenotype in E-cad+ conditions.

E-cad interacts with EGFR and induces hyper-activation of ERK
To further explore the mechanism by which E-cad expression leads to ERK activation and hyper-proliferation in breast cancer cells, we designed a bilateral mouse model. We injected E-cad+ and E-cad− cell pairs into the mammary fat pad of NOD-SCID Gamma (NSG) mice utilizing bilateral injection to allow for a direct comparison of tumor size in each animal (Fig. 3a). In all three tested cell pairs, we observed that E-cad+ tumors grew significantly more rapidly than E-cad− tumors, regardless of the endogenous E-cad expression in the parental cells (Fig. 3b–d). Specifically, we observed a three-fold increase in the growth rate in E-cad+ KI MDA-MB-231 tumors (Fig. 3b). For both MDA-MB-468 and MCF7 cell pairs, E-cad− tumors were already significantly smaller compared to E-cad+ control tumors three weeks after injection (Fig. 3c, d). In the MDA-MB-231 bilateral study, the average weight of final E-cad+ tumors was tenfold higher than the weight of E-cad− tumors (Fig. 3b, Extended Data Fig. 3a). This

is remarkable considering that wild-type (endogenously E-cad−) MDA-MB-231 cells already grow rapidly in vivo and are widely used for that reason [27, 37]. Similar trends were observed for MDA-MB-468 and MCF7 cell pairs (Fig. 3c,d, Extended Data Fig. 3b, c). We repeated the MDA-MB-231 study with a single tumor per mouse to ensure there was no crosstalk between the two implanted tumors and confirmed the results of the bilateral study (Extended Data Fig. 3d).

Immunohistochemistry (IHC) analysis of sections of MDA-MB-231 tumors from the bilateral study indicated that E-cad+ tumors displayed much higher levels of phospho-ERK and increased expression of proliferation marker Ki67 compared to E-cad− tumors (Fig. 3e). The regions of the tumor with high levels of expression of phospho-ERK and Ki67 correlated with the regions of the tumor with high levels of E-cad expression (Fig. 3f). Furthermore, we performed western blot analysis of the paired tumors from the bilateral study and found that the level of phospho-ERK was significantly higher in E-cad+ tumors compared to E-cad− tumors, with no significant change in total ERK (Fig. 3g). This data suggests that E-cad expression impacts tumor growth by inducing cancer cell hyper-proliferation via ERK phosphorylation.

Increased ERK activation may not be the only mechanism underlying hyper-proliferation in E-cad+ breast tumors. Hence, we conducted global and phosphosite proteomic analysis on MDA-MB-231 tumor pairs to assess all pathways activated by E-cad expression (Extended Data Fig. 3e). We designed this combined analysis to directly compare E-cad+ vs. E-cad− tumors obtained from the same mouse. A total of 7766 global proteins and 7258 phosphosites were identified. Using a cut-off of 1.5-fold relative expression change, we observed a ~15% increase in global proteins expressed and ~8% increase in activation sites in E-cad+ tumors compared to E-cad− tumors (Extended Data Fig. 3f). We first used this data to confirm previous results of MAPK pathway activation correlating with E-cad expression and sought to map the effect more fully (Fig. 3h). Global proteomic analysis of the MAPK pathway revealed a biologically significant (i.e. > 1.5, red-colored boxes) fold increase of proliferation marker Ki67 and EGFR, as well as transcription factors downstream of ERK, including FOS-related genes FOSL1/ FOSL2 and c-Myc (encoded by MYC) (Fig. 3h, i). RT-qPCR confirmed that FOS was also the most upregulated gene in the MAPK pathway at the mRNA level (Fig. 2a). Phosphoproteomic analysis showed significant increases in the phosphorylation abundance of key activation sites in the MAPK pathway: Y1172 and T693 on EGFR, Y204 and Y187 on ERK1/2 and S62 on c-MYC (Fig. 3h, i).

Next, we sought to determine if the MAPK and WNT pathways were the most changed when E-cad expression was manipulated. Utilizing the pathway analytical tools DAVID and KEGG, we found that the MAPK and WNT signaling pathways were among the most highly upregulated cancer-related pathways, which was one of the most upregulated pathway groups as determined by functional annotation (Extended Data Fig. 3g, h) [35–39]. These assessments indicate that activation off the MEK/ERK cascade is the driving force behind this hyper-proliferative phenotype induced by E-cad expression. The various protein and phosphosite changes around the ERK complex revealed by global and phosphosite proteomic analysis were confirmed via western blots of organoid samples (Extended Data Fig. 3i, Fig. 2e, f, Extended Data Fig. 2f,g).

With evidence that the MAPK pathway is the main driver of this hyper-proliferative phenotype associated with E-cad expression, we more closely examined cell membrane receptors that feed into the ERK cascade. Global and phosphosite proteomics revealed that the cell receptor EGFR was increased 1.4-fold in E-cad+ breast tumors compared to E-cad− tumors, and its phosphosites Y1172 (via EGFR auto-activation) and T693 (via ERK1/2) were upregulated 1.8-fold and 1.6-fold, respectively (Fig. 3i). Phosphosite Y1172 is
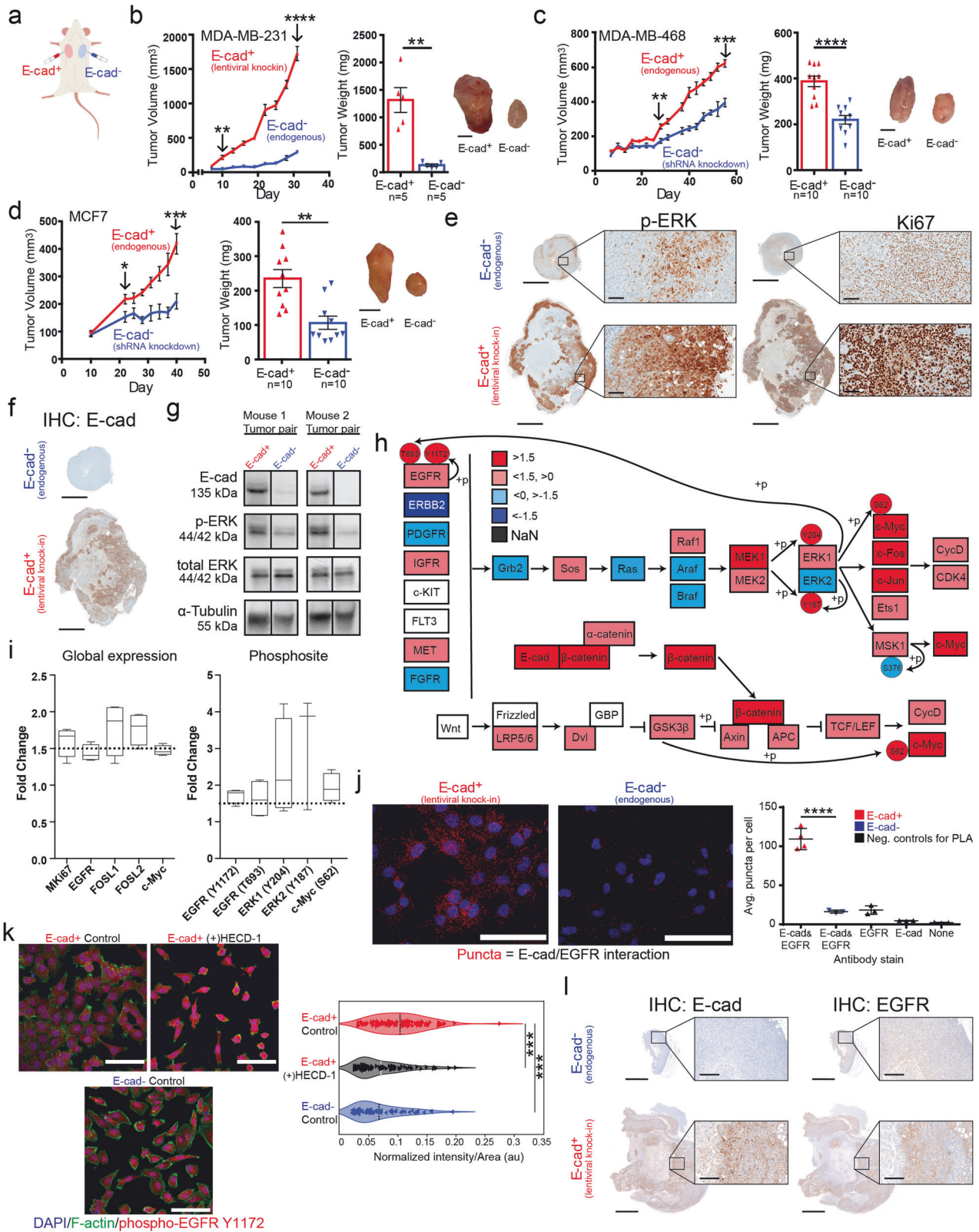
associated with EGFR auto-phosphorylation and phosphosite T693 is activated via a feedback loop of ERK1/2 signaling [12, 23]. Hence, we hypothesized that E-cad-induced EGFR auto-phosphorylation via crosstalk between EGFR and E-cad receptors at the cell membrane, increasing activation of the ERK cascade in MAPK and culminating in the hyper-proliferative phenotype of E-cad+ cancer cells.

To assess the putative interaction between E-cad and EGFR receptors, we conducted a proximity ligation assay (PLA) and quantified the number of cellular interactions between these

Fig. 3 E-cadherin expression correlates with increased proliferation and activation of MAPK pathway. a Schematic of bilateral mammary fat pad injection for in vivo modeling of primary tumor growth. Time-dependent tumor volume growth and final tumor weight of control MDA-MB-231 scramble and E-cad+ MDA-MB-231 tumors (****P < 0.0001) (**b**), control MDA-MB-468 scramble and E-cad− shRNA MDA-MB-468 tumors (***P = 0.0009) (**c**), and control MCF7 scramble and E-cad− shRNA MCF7 tumors (***P = 0.0003) (**d**). Apparent tumor volume was assessed using calipers to measure *x* and *y* dimensions. Tumor weight at the end of the study with pictures of representative excised tumors. Scale bars, 1 mm. **P = 0.0079, ****P < 0.0001, **P = 0.0015 respectively. P-values determined from paired T.Test for mice, 2-tailed distribution. **e** IHC staining of MDA-MB-231 bilateral tumor pair for phospho-ERK and proliferative marker Ki67 in MDA-MB-231 primary tumor pair. Scale bar = 3 mm, inset = 100 μm. **f** IHC staining for E-cad in MDA-MB-231 tumor pair. Scale bar = 3 mm, inset = 100 μm. **g** Western blot of two sets of primary tumors from the MDA-MB-231 bilateral mouse model, showing increased levels of phospho-ERK in E-cad+ tumors. **h** MAPK and WNT pathway schematics of fold change comparing MDA-MB-231 E-cad+ tumor to E-cad− tumor. Expression differences of ± 1.5-fold change were considered biologically relevant. **i** Box plots: fold change of key proteins in the MAPK pathway at the global proteomics level and activation differences of key proteins in the MAPK pathway (phosphoproteomics data). **j** Proximity ligation assay results demonstrate MDA-MB-231 E-cad+ cells have many E-cad/EGFR interactions, visualized by red puncta. Scale bar = 50 μm. Plot of average puncta/cell counts in E-cad+ and E-cad− cells, as well as in experimental negative controls (E-cad+ cells with single or no antibodies). N = 2, n = 2 to 4. **k** Immunofluorescence staining of phospho-EGFR at site Y1172 in E-cad+ control and HECD-1 (functional blocking antibody) treated cells. Nuclear expression is unchanged, but cytoplasmic expression is decreased in HECD-1 treated E-cad+ cells. N = 3, n = 3. **l** EGFR and E-cad IHC in MDA-MB-231 E-cad− and E-cad+ bilateral tumors, demonstrating overlap of stains, providing evidence for interactions between the two transmembrane proteins. Scale bar = 2 mm, zoom = 300 μm.

two proteins via immunofluorescence imaging. The PLA data provides strong evidence that interactions occur between E-cad and EGFR in E-cad+ cancer cells, which had an average of 129 puncta compared to an average of <20 puncta in E-cad− cancer cells (Fig. 3j and Extended Data Fig. 3j). For puncta (red signal) to be produced in this assay, the distance between the antibodies, and thus the proteins, cannot exceed 15-40 nm [40]. We also assessed the protein level of EGFR in organoids and observed significantly more EGFR in E-cad+ organoids compared to E-cad− organoids (Extended Data Fig. 3i). We also stained untreated control and HECD-1-treated E-cad+ cells with an antibody against phospho-EGFR Y1172 and demonstrated that functionally blocking E-cad disrupted EGFR activation, as there was less phospho-EGFR at the cell membrane in E-cad+ cells treated with E-cad functional blocking antibody HECD-1 (Fig. 3k, Extended Data Fig. 3k). To further confirm the co-localization of EGFR and E-cad, we conducted IHC staining on MDA-MB-231 E-cad+ and E-cad− tumors and observed similar staining patterns on the tumor samples for both antibodies (Fig. 3l), providing further evidence these two proteins are co-expressed. Together these results show a functional relationship between E-cad and EGFR signaling, as these receptors are in close proximity to each other at the cell membrane and disruption of E-cad intercellular junctions results in a decrease in EGFR activation at Y1172.

E-cadherin enhances metastatic outgrowth

In addition to the role of E-cad in primary tumor growth, proliferation may also occur at metastatic sites, so we sought to assess the role of E-cad in metastatic outgrowth. We employed two models of metastasis to characterize how E-cad may impact metastatic outgrowth. We first utilized the chicken chorioallantonic membrane (CAM) assay, in which intravital microscopy can be used to track cells as they extravasate, colonize, and proliferate (Fig. 4a) [38, 41, 42]. To fully control the impact E-cad expression has on the cellular phenotype, we generated MDA-MB-231 cells that only express E-cad after receiving an extracellular stimulus. These tunable E-cad-zsGreen cells gain E-cad expression when activated by the cell-permeant high-affinity ligand Shield-1 [43]. We included three experimental conditions: (i) Cells that did not express E-cad (E-cad− cells and tunable E-cad cells treated with vehicle control DMSO), (ii) cells that expressed E-cad at all times (E-cad+ cells), and (iii) cells that did not express E-cad until after extravasation into the embryo (tunable cell line treated with Shield-1).

To ensure E-cad expression did not impact the colonization potential of cancer cells, we conducted an extravasation assay in the CAMs with all cell line conditions listed above (Extended

Data Fig. 4a, b). Fluorescent images of CAMs showed larger colonies in both embryos injected with E-cad+ cells and embryos injected with tunable cells treated with Shield-1, when compared to E-cad− cells and tunable cells treated with DMSO (Fig. 4b). When quantified, the E-cad+ conditions had a 1.5 to 2-fold increase in number of metastases present throughout the CAMs when compared to those lacking E-cad expression (Fig. 4c). Together, this data confirmed that E-cad expression impacted cancer cell growth after completion of the metastatic cascade, i.e., post-extravasation from vessels into embryo of CAM.

We designed another metastatic assay, the mouse tail vein injection model, in which cancer cells are "forced" to colonize the lung via direct injection of tumor cells into the tail vein (Fig. 4d). The lung is the most common site of metastasis for breast cancer in mice and is one of the most common sites in humans [37, 44]. We injected the same number of either E-cad+ or E-cad− breast cancer cells into the tail vein of NSG mice and assessed metastatic burden in the lung four weeks after injection. We chose an extended timeline to minimize effects of survival or colonization ability in our dataset and focus on metastatic outgrowth. Mice weights were tracked throughout the experiment to monitor animal health (Extended Data Fig. 4c). After 4 weeks, we observed significantly more macro-metastases in the lungs of mice injected with E-cad+ cells (Extended Data Fig. 4d). Quantification of metastatic burden (via RT-qPCR analysis of the human genomic marker *HK2*) showed a remarkable 109-fold increase in the relative expression in lungs of mice injected with E-cad+ cells compared to Ecad- cells (Fig. 4e) [39]. These results were confirmed via H&E staining of lung sections, where dense foci of cancer cells were present in the lungs of mice injected with E-cad+ cells (Fig. 4f). In contrast to E-cad− cells, we also observed a majority of the cells in the lungs of mice injected with E-cad+ cells were positive for Ki67 (Fig. 4g). Finally, we observed a significant increase in phospho-ERK expression in lungs from animals injected with E-cad+ cells and confirmed the tumor cells maintained E-cad expression at the metastatic site (Fig. 4g, Extended Data Fig. 4e). Among the subtypes of breast cancer, triple negative breast cancer (TNBC) has the highest rates of metastasis and the worst prognosis. We probed the TCGA invasive breast cancer (BRCA) dataset again, focusing on E-cad correlation with lung metastasis gene sets. Upon stratifying by subtype, CDH1 expression was correlated with genes involved in metastasis of breast cancer to the lung in basal BRCA (TNBC) dataset (Extended Data Fig. 4f). These results suggest that, in addition to its role in primary tumor growth, E-cad promotes metastasis via proliferation at the secondary metastatic site.
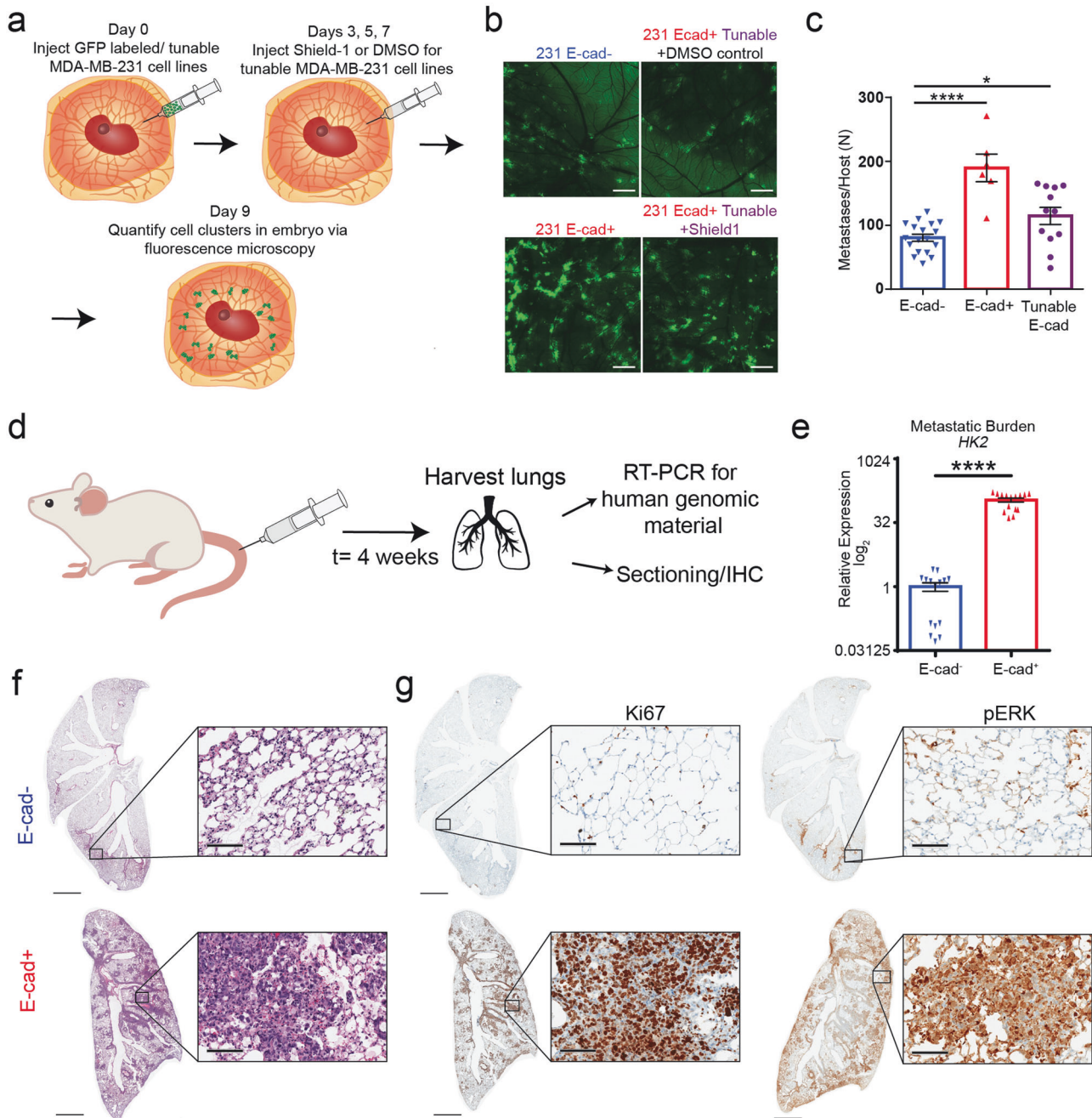
Fig. 4 E-cadherin results in larger metastatic burden in two in vivo models via MAPK proliferation pathway. a Schematic of intravital microscopy experiment using CAM assay. **b** Confocal images of embryos on day 18 of embryo growth (9 days post injection) showing greater accumulation of GFP tagged E-cad+ and Shield-1 treated tunable cells when compared to the scramble control (E-cad−) or DMSO treated tunable cells. ROI 6x6 tile, 10x objective. **c** Number of metastases per host quantified from fluorescent images. **d** Schematic of tail vein injection of breast cancer cells. **e** Relative expression level of *HK2* a marker of human genomic material comparing lungs of mice injected with E-cad+ to E-cad− cells. **f** H&E staining of lungs from E-cad+ and E-cad− mice. Scale bar = 2 mm. **g** IHC staining for Ki67 and phospho-ERK (respectively) in the lungs of from mice injected with E-cad+ and E-cad− MDA-MB-231 cells. Scale bar = 2 mm.

Blocking ERK phosphorylation reverses E-cad-induced cancer cell hyper-proliferation

To validate the above mechanism of action of E-cad and to test potential translation to clinical settings, we treated MDA-MB-231 E-cad+ tumor-bearing mice with MEK1/2 inhibitor PD0325901 (mirdametinib), selected from our in vitro drug screen (Fig. 5a). PD0325901 is highly specific to MEK1/2 kinase activity, without impacting MEK activation, and therefore, it is frequently used when studying ERK activity [32]. This MEK inhibitor is administered orally to patients and the dosage and scheme were determined based on clinical trials for solid breast tumors and preclinical in vivo models [45–47]. Mice were given 20mg/kg of PD0325901 for 5 days and then had 3 weeks off before the next treatment was given to ensure safety of the animals, given clinical indications of toxicity at high dosages [32, 48]. We monitored the weight of the animals throughout the study, as it would be the first sign of toxicity, and did not observe a significant impact on mouse weight with the 5-day administration protocol (Extended Data Fig. 5a).

Compared to vehicle control, we observed a significant decrease in tumor progression and final tumor weight/size
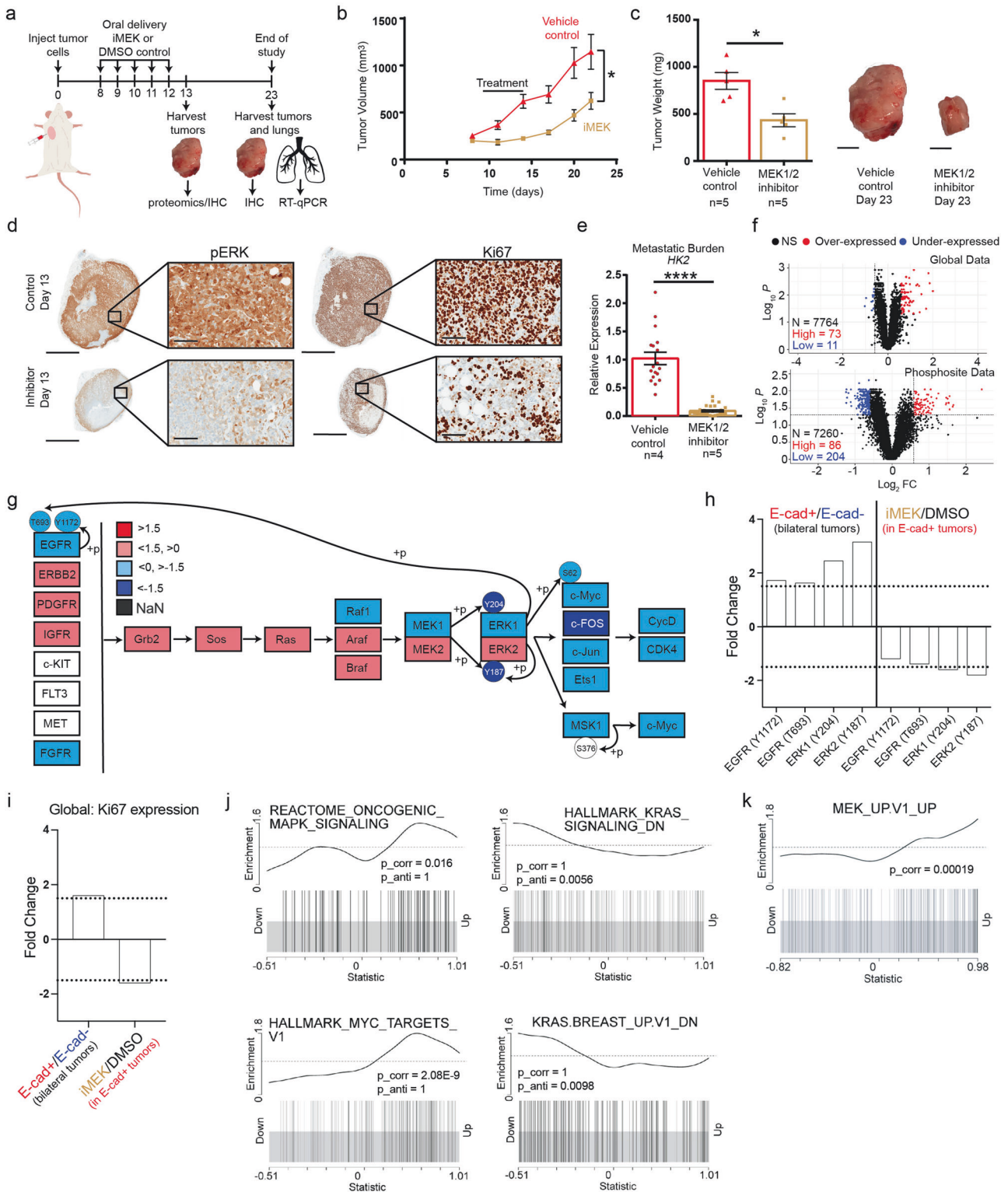
when mice bearing E-cad+ tumors were treated with PD0325901 (Fig. 5b, c, Extended Data Fig. 5b). After treatment ended on day 12, the growth curve of the treated tumors increased again, demonstrating prolonged administration is required for highest efficacy. With this rebound of growth in mind, we harvested tumors on day 13, the day after treatment ended, and observed the anticipated decrease in phospho-ERK and Ki67 levels via IHC staining (Fig. 5d). We note that for tumors harvested at the conclusion of the study (day 23), phospho-ERK and Ki67 levels were not significantly different in PD0325901 treated tumors compared to control (Extended Data Fig. 5c), further explaining the increase in tumor growth after treatment concluded on day 12. Hence, MEK inhibition via PD0325901, which prevents ERK activation, can slow E-cad+-induced tumor hyper-growth to match that of E-cad− tumor progression (Extended Data Fig. 5d).

Fig. 5 Blocking ERK phosphorylation stops hyper-proliferative effect of E-cad. a Schematic of orthotopic injection into mammary fat pad of NSG mice to assess impact of MEK1/2 inhibitor on primary tumor progression (N = 5 per group). **b** Time-dependent volume of MDA-MB-231 E-cad+ untreated (red line) and treated (gold line). Apparent tumor volume was assessed using calipers to measure x and y dimensions. *$P = 0.0345$. **c** Tumor weight at the end of the study with representative pictures of excised tumors. *$P = 0.0159$. Scale bar = 1 mm. **d** IHC staining of tumors harvested on day 13, 1 day after treatment was completed, showing downregulation of phospho-ERK with treatment of MEK1/2 inhibitor PD0325901. There is a significant decrease in Ki67 positive cells when mice were treated with MEK1/2 inhibitor PD0325901. Scale bar = 3 mm. Inset = 100 μm. **e** Relative expression level of *HK2* (marker for human genomic material) in the vehicle control and MEK1/2 inhibitor treated groups. ****$P < 0.0001$. N = 2, n = 3 per mouse for qPCR. **f** Volcano plots showing statistically significant fold increase/decrease during treatment in the global proteomics and phosphosite proteomics. **g** Pathway schematic comparing relative expression of treated tumors to control tumors. **h** Fold change of key phosphosites EGFR: Y1172 ($p = 0.08$, $p\_adj = 0.32$), T693 ($p = 0.00046$, $p\_adj = 0.005$) ERK: T185/Y187 ($p = 0.22$, $p\_adj = 0.51$), Y202/Y204 ($p = 0.65$, $p\_adj = 0.84$)), comparing treatment study with E-cad+ tumors to E-cad+/E-cad− bilateral tumor proteomics data (from Fig. 3), demonstrating reversion of phenotype induced by E-cad expression. **i** Fold change of Ki67 global protein level ($p = 0.0002$, $p\_adj = 0.01$), comparing E-cad+/E-cad− bilateral tumor proteomics data to iMEK treatment study with E-cad+ tumors, showing complete reversion of induced proliferation marker. **j** Enrichment plots for GSEA MAPK gene sets, including oncogenic MAPK signaling, were significantly correlated with CDH1 expression. Genes downregulated by KRAS signaling were anti-correlated with CDH1 expression. TCGA invasive breast cancer (BRCA) dataset was used. **k** Enrichment plot for the basal subset of BRCA, the predominant type of cells used in this manuscript, MEK signaling showed a positive correlation with CDH1 expression.

Table 4. GSEA MAPK gene sets, including oncogenic MAPK and KRAS correlation with *CDH1* (E-cad) expression (Enrichment plots in Fig. 5).

TCGA-BRCA dataset			
GSEA gene set	**Brief description**	**p-value for CDH1 expression being positively correlated with gene set signaling**	**p-value for CDH1 expression being anti-correlated with gene set signaling**
REACTOME_ONCOGENIC_MAPK_SIGNALING	Genes involved in oncogenic MAPK signaling.	0.016	1
HALLMARK_KRAS_SIGNALING_DN	Genes whose expression is down-regulated by KRAS activation.	1	0.0056
KRAS.BREAST_UP.V1_DN	Genes down-regulated in breast cancer cells over-expressing KRAS.	1	0.0098
HALLMARK_MYC_TARGETS_V1	Genes regulated by MYC signaling.	2.08E-09	1

We also assessed metastatic burden in the lungs using RT-qPCR and observed a 90-fold decrease in relative expression of *HK2* when mice were treated with the MEK1/2 inhibitor compared to control mice (Fig. 5e) [39]. Hence, we believe either MEK1/2 treatment prevents metastasis from the primary tumor as well as further growth of cells that metastasized prior to the start of treatment. Additionally, our data in Fig. 4g shows phospho-ERK positive cells in mice lungs from the E-cad+ condition of the tail vein experiment. Hence, when at a secondary site, E-cad+ breast cancer cells utilize the same proliferative pathway that we observe in the E-cad+ primary breast tumor.

To ensure that the inhibitor PD0325901 worked specifically and did not significantly impact other pathways, we conducted global and phosphosite proteomics on the treated and untreated tumors. We observed that the expression of only ~1% of proteins and ~4% of phosphosites were impacted by PD0325901 treatment when comparing treated to control E-cad+ tumors, further demonstrating the high specificity of our chosen inhibitor (Fig. 5f). We observed a biologically significant fold decrease (<1.5) in the expression of downstream transcription factor FOS as well as phosphosites Y187 and Y204 on ERK when comparing PD0325901 treated mice to control mice (Fig. 5g). Analysis of the phosphosite data confirmed that in addition to preventing phosphorylation of ERK by MEK1/2 at sites Y187 and Y204, PD0325901 treatment also resulted in decreased phosphorylation of Y1172 and T693 on EGFR (Fig. 5h). We also observed a significant fold decrease in proliferation marker Ki67 in E-cad+ tumors treated with PD0325901 (Fig. 5i). These results are also in agreement with the data obtained from our 3D organoid model, which shows reduced phospho-ERK (Extended Data Fig. 2f) and EGFR expression (Extended Data Fig. 3i) in PD0325901 treated organoids. This

data demonstrates the pathway is preserved in vivo, in addition to the response to treatment.

The MAPK pathway downstream of E-cad expression delineated in this manuscript to be both in vitro (Figs. 2a and 3h–j) and in vivo (Fig. 5f–i), was also implicated in the invasive breast cancer TCGA dataset (Fig. 5j, Table 4). MAPK and MYC gene sets, including oncogenic MAPK signaling, were significantly positively correlated with *CDH1* expression (Fig. 5j). Additionally, genes downregulated by KRAS signaling are anti-correlated with *CDH1* expression, indicating further regulation of MAPK signaling by E-cad. For the basal subset of BRCA (TNBC samples) - the focus of this manuscript, MEK and ERK signaling showed positive correlations with *CDH1* expression (Fig. 5k, Table 5), although ERK signaling is just short of statistical significance. Thus, patients with higher E-cad (*CDH1*) expression are associated with increased MAPK (MEK/ERK) signaling. This final piece of clinical data provides strong evidence the observed mechanism in our in vitro multi-compartment tumor organoid model and various pre-clinical animal studies is also valid in the clinical setting.

DISCUSSION
E-cadherin has traditionally been classified as an EMT marker whose loss is correlated with successful cancer metastasis [1–4]. Because of this association, E-cad has been classified as a tumor suppressor gene. However, when examining breast cancer clinical data, this mechanistic classification contradicts the fact that patients with E-cad positive invasive breast tumors have reduced overall survival rates [11]. Additionally, E-cad (*CDH1*) expression is correlates with both metastatic and proliferation gene sets when examining the TCGA invasive breast carcinoma (BRCA) RNA-seq

Table 5. Basal subset of BRCA, the predominant type of cells used in this manuscript, MEK signaling showed a positive correlation with CDH1 expression (Enrichment plots in Fig. 5).

TCGA-BRCA basal dataset		
GSEA gene set	**Brief description**	**p-value for CDH1 expression being positively correlated with gene set signaling**
MEK_UP.V1_UP	Genes up-regulated in breast cancer cells over-expressing MAP2K1.	0.00019
REACTOME_MAPK3_ERK1_ACTIVATION	Genes up-regulated following MAPK3 (ERK1) activation.	0.078

dataset. Here we assessed the role of E-cad in breast tumor progression as a driver of cancer cell proliferation utilizing our recently developed multi-compartment tumor organoid model and multiple in vivo models. This study identified a previously unknown link between E-cad and the proliferation-based MAPK cascade that has never before been delineated in cancers. Our findings reconcile the paradoxical role of E-cad in literature with its correlation with poor prognosis in clinical data. E-cad loss would drive invasive behavior and EMT, leading to more metastasis. However, E-cad expression strongly activates the MEK/ERK cascade, leading to increased proliferation – the driving force behind the highly aggressive nature of E-cad positive IDC breast tumors. Clinical data corroborates our findings, as E-cad (CDH1) expression is correlates with increased MAPK signaling in the invasive breast carcinoma (BRCA) RNA-seq TCGA dataset.

Due to its mechanical role in cell-cell adhesion, it was imperative to study E-cad in a biologically relevant environment, ensuring E-cad can create adherens junctions in all three directions rather than limiting E-cad to planar interactions in standard 2D culture conditions. Utilizing a 3D multi-compartment organoid system, we observed large proliferation changes using engineered cancer cell pairs [24]. In animal models, we observed that E-cad expression correlated not only with increased primary tumor growth, but also with increased metastatic outgrowth. This data suggests that although E-cad has implications in the migratory and invasive phenotypes of cancer cells, this cell-cell adhesion protein also influences proliferation at both primary and secondary sites in the orthotopic IDC models using NSG mice.

Our phosphoproteomic assessment identified ERK1/2 activation through the MAPK signaling cascade as the molecular mechanism contributing most to this dramatic change in proliferation. This link between E-cad expression and ERK signaling is supported by studies conducted in normal mammary epithelial cells, in which researchers observed ligated E-cad can recruit EGFR, induce its ligand-independent activation, and result in activation of the MAPK pathway [14, 23, 33]. We identified MEK1/2 phosphorylation of ERK at Y204 and Y187 and auto-phosphorylation of EGFR at Y1172 as the key E-cad-dependent activation sites in the MAPK pathway. Phosphosite Y1172 on EGFR is activated in the presence of EGF or similar stimulus, like soluble E-cad, in normal mammary epithelial cells and has been linked to auto-phosphorylation behavior of EGFR at this phosphosite, providing further proof that these proteins are likely to interact and cause upregulation of the specific phosphorylation site Y1172 [13, 18–20, 23]. EGFR activated on Y1172 can feed into either the MAPK or PI3K pathway, resulting in changes in cell cycle, growth, proliferation, metabolism, etc [13, 14, 17, 23]. Our proteomics assessment allowed us to mechanistically connect these disparate observations and demonstrate that the ERK cascade in MAPK pathway is the main driver behind the hyper-proliferative phenotype we observed in E-cad+ breast cancer cells.

Functional blocking of the E-cad–EGFR interaction resulted in localization changes of phospho-ERK, which became more abundant in the nucleus, as well as accumulation of phospho-EGFR (site Y1172) in the nucleus rather than at the cell membrane.

These results indicate E-cad must be functional for EGFR to be stimulated and undergo auto-phosphorylation; thus, providing further evidence of a functional crosstalk between cadherins and RTKs exists in cancer [13, 18–20, 23]. These results also provide evidence of the downstream impacts these cell surface interactions have on tumor progression – causing breast tumors to enter a state of hyper-proliferation [13, 18–20, 23].

Pharmacological inhibition of MEK1/2 kinase activity by employing MEK inhibitor PD0325901 resulted in decreased levels of phosphorylated ERK1/2 and blocking this activation event was sufficient to reverse this hyper-proliferative effect in vitro and in vivo. In our studies, MEK inhibitor PD0325901 reverted E-cad+ primary tumor growth to that of E-cad− tumors and decreased metastatic burden in the lungs. Employment of inhibitors specifically targeting the MEK1/2 kinase activity hold potential as a treatment option for E-cad positive breast tumors; although, delivery is an obstacle due to the side effects and off target impacts of MEK inhibitors on other organs and areas of the body. Clinical trials for PD0325901, previously tested for efficacy in treating solid tumors of the breast and melanoma, had to be terminated due to toxicity concerns and severe side effects [32, 45–48]. However, MEK inhibitors are only approved for combination treatment of a specific subset of melanoma. Our work suggests that patients with E-cad+ breast tumors could benefit from treatment with MEK inhibitors, and future studies should explore how to safely administer MEK inhibitors with traditional chemotherapeutics employed against invasive breast carcinoma.

Clinical data examining IDC breast cancer patients, which accounts for 80% of all breast cancers, and of which 90% are E-cad+, corroborates our results: patients with high E-cad expression have a worse overall survival [11]. When we couple this clinical dataset from Metabric with both a correlation analysis of E-cad to metastasis and proliferation associated genes and to MAPK signaling within the TCGA invasive breast carcinoma (BRCA) RNA-seq dataset, we demonstrate that the results and the underlying mechanism described here extend to the clinical settings. Here we identify a molecular mechanism responsible for these observations and a therapeutic target with implications that begin but do not end with breast cancer.

MATERIALS AND METHODS
Cell culture
Human breast carcinoma cells MDA-MB-231, MCF7, MDA-MB-468, (ATCC) were cultured in Dulbecco's modified Eagle's medium (DMEM, 10-013-CV, Corning) supplemented with 10% (v/v) fetal bovine serum (FBS, 35-010-CV, Corning) and 1% penicillin–streptomycin (15140-122, Gibco). Cells were maintained at 37 °C and 5% CO_2 in a humidified incubator during cell culture and regularly tested for mycoplasma contamination (Lonza MycoAlert).

Lentivirus production and transduction
HEK-293T cells (ATCC) were cultured in Dulbecco's modified Eagle's medium (DMEM, Corning) supplemented with 10% (v/v) fetal bovine serum (FBS, Corning) and 1% Penicillin-Streptomycin (Gibco). Mission shRNA glycerol stock for CDH1 (NM004360, TRCN0000237841) was

Table 6. List of antibodies used in immunofluorescence, immunohistochemistry, and western blots.

Antibody	Company	Ref/product #	Lot #
E-cadherin	CST	24E10/31952	15
E-cadherin	CST	4A2/14472S	8
Beta-catenin	CST	D10A8/8480S	9
phospho-ERK (phospho-p44/42 MAPK)	CST	9101S	31
T-ERK (p44/42 MAPK)	CST	L34F12/4696S	29
pMEK	CST	41G9/9154S	27
T-MEK	CST	L38C12/4694S	2
Alpha tubulin	CST	11H10/21215S	11
GAPDH	CST	D4C6R/97166S	6
Beta-catenin	Sigma	SAB4200720	096M478V
phospho-EGFR (Y1172)	Cusabio	CSB-PA007951	G1009Y
EGFR	CST	D38B1/4267S	24
Ki67	CST	8D5/9449S	12
Cleaved-caspase 3	CST	D175/9661s	47

obtained from Sigma. Bacterial culture was started and incubated for 16 h (overnight) on a shaker at 37 °C at a speed of 200 RPM. Plasmid DNA was extracted using Midi-Prep Kit from (740412.50, Machery-Nagel). Calcium chloride (2M) and HEPES-buffered-saline were used for transfection and lentiviral production. Plasmid DNA and reagents were added to HEK-293T cells and virus was harvested every 24 h for 3 days. E-cadherin positive cells (MCF7, MDA-MB-468) received two rounds of virus for a total period of 48 h. After 48 h, cells were given fresh DMEM. After 24–48 h, cells were given DMEM with 5 µg/mL puromycin (Gibco) for selection. Knockdown cells were cultured in puromycin conditioned medium for three days before checking protein expression. Cells were kept in selection medium for the duration of the experiments. Lentiviral knock-in of MDA-MB-231 (endogenously no E-cad expression) was generated as previously described [49]. Briefly, the lentiviral vector of E-cadherin-EGFP was generated from EGFP; pCS-CG (Addgene) via cloning full-length E-cadherin upstream of EGFP between the Nhe1 and Age 1 sites of pCS-CG to generate an EGFP-fused protein [49].

2D immunofluorescence staining and imaging
Cells were seeded at desired density in 96-well flat-bottom plate. After 24 h growth, 4% paraformaldehyde (Sigma) was added to each well to fix cells and removed after 20 min incubation at room temperature. After washes with DPBS, 0.1% Triton (Sigma) was added to cells to permeabilize the cell membrane and incubated for 5 min at room temperature before removal. Wells were then blocked with 5% Normal Goat Serum (NGS) (Sigma) for 1 h. Primary antibodies were added, and samples were incubated overnight in a 2–8 °C fridge. After removal of the primary antibodies (see Table 6), samples were stained with secondary antibodies in 1% NGS for 30 min at room temperature. Samples were then stained with H33342 (nuclear DNA, ThermoFisher) and phalloidin (F-actin, Invitrogen) in 1% NGS for 15 min at room temperature. Samples were then washed 3× with DBPS (Corning) before imaging. Confocal images were captured using a 40× oil objective and Nikon A1 Confocal microscope [50]. Experiments for β-catenin localization: $N = 3$, $n = 3$. Immunofluorescence analysis of phospho- ERK ($N = 2$, $n = 3$) and phospho-EGFR ($N = 2$, $n = 3$) was conducted by a CellProfiler™ pipeline. Briefly, nuclei and their corresponding cell bodies were masked from the DAPI and phalloidin channels respectively [51]. These masks were applied to the biomarker channel to elicit spatial expression at single-cell resolution.

Organoid modeling
A multi-compartment organoid model was generated with Matrigel (Corning) and rat tail type I (Corning) [24]. Cells were trypsinized, pelleted, and resuspended in Matrigel at the desired cell density and then wrapped in a collagen I gel was mixed as previously described by Fraley et al. [52].

The organoids are plated in a 96-well round-bottom dish and suspended in 200 µL medium.

Organoid immunofluorescence staining and imaging
Organoids were harvested at various time points, washed 3× in DPBS (Corning) and then fixed in 4% paraformaldehyde (Sigma) overnight at 4 °C. Organoids were rinsed with DPBS prior to capturing DIC images using Nikon A1R confocal microscope ($N = 3$, $n = 3$). Organoids to be stained with antibodies were permeabilized with 0.1% Triton-X (Sigma) for 10 min. Organoids were then washed with DPBS and blocked with 5% NGS (Cell Signaling Technology) for 1 h. Primary antibodies were added at 1:100 dilution and incubated overnight at 4 °C. Following primary antibody incubation, organoids are washed 3× in DPBS and then stained with secondary antibodies (Invitrogen) as well as F-actin/phalloidin (Invitrogen) and Hoechst 3342 (ThermoFisher) in 1% NGS for 1 h at room temperature. After fluorescent stain incubation, organoids are washed 3x with DPBS and then incubated in tissue clearing solution (60% glycerol, 2.5 M fructose in DI water) for 20 min at room temperature. Organoids were washed 3× before imaging on Nikon AX confocal microscope using 20× water immersion objective and 40× water immersion objective.

2D and 3D proliferation using PrestoBlue viability assay
Cells were seeded in 96-well plate at 2000 cells/well for MDA-MB-231 and MCF7 and at 5000 cells/well for MDA-MB-468 (day 0). On day 1 and day 7, cells were incubated in 1x PrestoBlue (ThermoFisher) at 37 °C for 1 h. To account for background signal, 5–10 wells of 1× PrestoBlue were prepared and measured to subtract off background medium signal from the experimental wells. After reading the signal, cells were washed with DPBS 3×, given 100 µL of fresh medium. $N = 3$ biological repeats. $*P = 0.01$, $**P = 0.003$, $***P = 0.0002$

Organoids were incubated at 37 °C in a 1× PrestoBlue for 3 h on day 1 (day of generation). Standard curves were generated relating cell number to RFU to ensure linear relationship (Extended Data Fig. 1e, f). After reading, organoids were wash in DBPS 5× and given 200 µL of fresh medium. Experiment was carried out for either 5 or 8 days. To account for background signal, 5–10 wells of 1× PrestoBlue were prepared and measured. The average background signal value was subtracted from the experimental wells. SpectraMax plate reader (Molecular Devices) was used to read the RFU for all experiments at (EX 540, EM 600, cutoff 590). $N = 3$ biological replicates for all cell lines: MDA-MB-231 ($n = 60$) $****P \leq 0.0001$, MDA-MB-468 ($n = 60$) $**P = 0.0073$, and MCF7 ($n = 50$) $***P = 0.0008$. All data are mean ± SEM. Statistical test used: Mann–Whitney test, two sided for 2D cells and organoids.

mRNA extraction and cDNA synthesis
Organoids were generated and then incubated in fresh media. After 24 h, organoids were harvested and washed 3× in DPBS (Corning). To isolate mRNA, TriZol reagent (Invitrogen) was added to the washed organoids and then vortexed until completely dissolved. Direct-zol Mini Prep kit (Zymo research) reagents and protocol were used to complete RNA extraction. cDNA was synthesized using the iScript cDNA kit (BioRad) following the recommended protocol to make 1000 ng of cDNA for a total reaction volume of 20 µL.

RT-qPCR
qPCR was conducted with iTaq-SYBR Green (Bio-Rad) using the Bio-Rad CFX CFX384 Touch Real-Time PCR detection system. Primers were obtained from Integrated DNA Technologies and are listed in Table 7 and Table 8. For pathway analysis, $N = 3$ biological replicates, $n = 3$ technical replicates. P-values calculated via T.Test (2 tailed, equal variance). For analysis of harvested mouse tissues via $HK2$ expression, $N = 5$ and all data are mean ± SEM. P-values determined Mann–Whitney test, two sided.

Inhibitor studies
Inhibitor studies were conducted using the organoids described above. Experiments were carried out for a week and imaged daily using phase contrast microscopy. Inhibitors listed in Table 3 were obtained from Selleckchem and fresh or conditioned medium (containing the drug) was added on the day the organoids were generated and not changed during the week-long experiment. For small-molecule screen, $N = 1$, $n = 5$. All data are mean ± SEM. P-values determined via ANOVA. For IC$_{50}$ curves, $N = 3$, $n = 5$ for PD0325901 and Trametinib.

Table 7. List of primers used to assess MAPK and WNT signaling pathways in the organoid system.

AKT1 FWD	AGCGACGTGGCTATTGTGAAG
AKT1 RVS	GCCATCATTCTTGAGGAGGAAGT
ATF2 FWD	AATTGAGGAGCCTTCTGTTGTAG
ATF2 RVS	CATCACTGGTAGTAGACTCTGGG
DAXX FWD	GATACCTTCCCTGACTATGGGG
DAXX RVS	GTAACCTGATGCCCACATCTC
ELK1 FWD	CTGCCTCCTAGCATTCACTTC
ELK1 RVS	GCTGCCACTGGATGGAAACT
FOS FWD	CCGGGGATAGCCTCTCTTACT
FOS RVS	CCAGGTCCGTGCAGAAGTC
GREB1 FWD	ATGGGAAATTCTTACGCTGGAC
GREB1 RVS	CACTCGGCTACCACCTTCT
JUN FWD	TCCAAGTGCCGAAAAAGGAAG
JUN RVS	CGAGTTCTGAGCTTTCAAGGT
JUND FWD	TCATCATCCAGTCCAACGGG
JUND RVS	TTCTGCTTGTGTAAATCCTCCAG
MAP2K1 FWD	CAATGGCGGTGTGGTGTTC
MAP2K1 RVS	GATTGCGGGTTTGATCTCCAG
MAP2K2 FWD	AGGTCCTGCACGAATGCAA
MAP2K2 RVS	CGTCCATGTGTTCCATGCAA
MAP2K3 FWD	GAGGGAGACGTGTGGATCTG
MAP2K3 RVS	CCGCACGATAGACACAGCAAT
MAP2K4 FWD	TGCAGGGTAAACGCAAAGCA
MAP2K4 RVS	CTCCTGTAGGATTGGGATTCAGA
MAP2K5 FWD	CCGGACCCTCTCAACACAG
MAP2K5 RVS	ATGACCAAGAGTGTCCCGATA
MAP2K6 FWD	AAACGGCTACTGATGGATTTGG
MAP2K6 RVS	CAGTGCGCCATAAAAGGTGAC
MAPK1 FWD	TCACACAGGGTTCCTGACAGA
MAPK1 RVS	ATGCAGCCTACAGACCAAATATC
MAPK13 FWD	TGAGCCGACCCTTTCAGTC
MAPK13 RVS	AGCCCAATGACGTTCTCATGC
MAPK14 FWD	TCAGTCCATCATTCATGCGAAA
MAPK14 RVS	AACGTCCAACAGACCAATCAC
MAPK3 FWD	CTACACGCAGTTGCAGTACAT
MAPK3 RVS	CAGCAGGATCTGGATCTCCC
MAPK8 FWD	TCTGGTATGATCCTTCTGAAGCA
MAPK8 RVS	TCCTCCAAGTCCATAACTTCCTT
MAPK9 FWD	GAAACTAAGCCGTCCTTTTCAGA
MAPK9 RVS	TCCAGCTCCATGTGAATAACCT
APC FWD	AAGCATGAAACCGGCTCACAT
APC RVS	CATTCGTGTAGTTGAACCCTGA
AXIN1 FWD	GGTTTCCCCTTGGACCTCG
AXIN1 RVS	CCGTCGAAGTCTCACCTTTAATG
BTRC FWD	TGCCCAAGCAACGGAAACT
BTRC RVS	GCCCATGTTGGTAATGACACA
CCND1 FWD	GCTGCGAAGTGGAAACCATC
CCND1 RVS	CCTCCTTCTGCACACATTTGAA
CSNK1A1 FWD	AGTGGCAGTGAAGCTAGAATCT
CSNK1A1 RVS	CGCCCAATACCCATTAGGAAGTT
CSNK2A1 FWD	CGAGTTGCTTCCCGATACTTC

Table 7. continued

CSNK2A1 RVS	ACTTGCCAGCATACAACCCAA
CTBP1 FWD	CGACCCTTACTTGTCGGATGG
CTBP1 RVS	TTGACGGTGAAGTCGTTGATG
CTNNB1 FWD	AGCTTCCAGACACGCTATCAT
CTNNB1 RVS	CGGTACAACGAGCTGTTTCTAC
DVL1 FWD	GAGGGTGCTCACTCGGATG
DVL1 RVS	GTGCCTGTCTCGTTGTCCA
FZD1 FWD	ATCTTCTTGTCCGGCTGTTACA
FZD1 RVS	GTCCTCGGCGAACTTGTCATT
GSK3B FWD	GGCAGCATGAAAGTTAGCAGA
GSK3B RVS	GGCGACCAGTTCTCCTGAATC
HDAC1 FWD	CTACTACGACGGGGATGTTGG
HDAC1 RVS	GAGTCATGCGGATTCGGTGAG
LEF1 FWD	AGAACACCCGATGACGGA
LEF1 RVS	GGCATCATTATGTACCCGGAAT
NLK FWD	CCAACCTCCACACATTGACTATT
NLK RVS	ACTTTGACATGATCTGAGCTGAG
PPARD FWD	GCCTCTATCGTCAACAAGGAC
PPARD RVS	GCAATGAATAGGGCCAGGTC

Table 8. List of primers used to assess metastatic burden (*HK2*).

18s Human FWD	AGAAGTGACGCAGCCCTCTA
18s Human RVS	GAGGATGAGGTGGAACGTGT
18s Mouse FWD	CGGCGACGACCCATTCGAAC
18s Mouse RVS	GAATCGAACCCTGATTCCCCGT
aTubulin Human FWD	AGGAGTCCAGATCGGCAATG
aTubulin Human RVS	GTCCCCACCACCAATGGTTT
aTubulin Mouse FWD	CACACAAGCTCACTCACCCT
aTubulin Mouse RVS	CTGTTATTAGGGATGTGACTCCA
HK2 (Human) FWD	CCAGTTCATTCACATCATCAG
HK2 (Human) RVS	CTTACACGAGGTCACATAGC
GAPDH Human FWD	GGAGCGAGATCCCTCCAAAAT
GAPDH Human RVS	GGCTGTTGTCATACTTCTCATGG
GAPDH Mouse FWD	TCACCACCATGGAGAAGGC

Quantifying multi-compartment organoid volume
Inner and outer layers of the organoids were manually traced using NIS Elements software to generate a radius measurement. Volume of inner and total organoid was calculated using the volume for a sphere: $V = 4/3 \ \pi r^3$. To calculate the volume of the collagen layer, the inner volume was subtracted from the total volume. $N = 1$, $n = 5$. All data are mean ± SEM. *P*-values determined via ANOVA.

Protein extraction, concentration, and western blot assays
A clear sample buffer containing SDS with protease inhibitor (05892970001, Roche) was used to lyse 10–15 organoids or 2D cells via cell scraping method from a confluent 10 cm dish. Samples were sonicated for 10–15 pulses using a needle probe sonicator (VWR Scientific). Samples were then heated at 100 °C for 5 min to completely denature the protein. Protein samples were stored in −80 °C freezer until ready for use. Protein concentration was measured using MicroBCA Kit (23235, ThermoFisher) following the manufacturer's protocol. A loading buffer made from 2× Laemlli (Bio-Rad) was prepared with the instructed amount of beta-mercaptoethanol (Gibco) and added to the protein samples for a final concentration of 2 µg/µL. Bio-Rad mini-protean gels (4–15% gradient, 4561086) were used for gel

electrophoresis. Transblot Turbo packs (Bio-rad) were used to transfer the protein from the gel to PVDF membrane. Antibodies are listed in Table 6 and recommended dilutions for the primary and secondary antibodies were used in incubations. Blots were imaged using Bio-Rad imager.

Functional blocking experiment

MDA-MB-231 E-cad− and E-cad+ cells were plated in 96-well glass bottom dish at 5000 cells/well. Wells were coated with collagen (50 µg/mL) prior to seeding the cells. HECD-1 (Invitrogen, 13-1700) was used to functionally block E-cad in MDA-MB-231+Ecad cells. The control and treated wells were imaged using live cell microscopy (Nikon Ti2) to track their migration patterns for the 4 h incubation. After the 4 h migration study, cells were rinsed 1x with DBPBS and fixed with 4% PFA for 20 min at room temperature. After fixation, wells were stained for various primary antibodies (Table 6). Wells were prepared for imaging as described above and images were captured using a Nikon A1 confocal and 40× oil objective. Immunofluorescence analysis was conducted by a CellProfiler pipeline. Briefly, nuclei and their corresponding cell bodies were masked from the DAPI and phalloidin channels respectively. These masks were applied to the Biomarker channel to elicit spatial expression at single-cell resolution. $N = 3$ biological replicates, $n = 4$ technical replicates. All data are mean ± SEM. P-values determined Mann–Whitney test, two sided.

Mouse models

All mouse experiments were carried out according to protocols approved by the Johns Hopkins University Animal Care and Use Committee in accordance with the NIH Guide for the Care and Use of Laboratory Animals. All mice were housed at a temperature of 25 °C under a 12 h dark/light cycle.

For the bilateral studies. Primary tumors were established with cell lines obtained from ATCC. Cells were cultured in 5% CO_2 and 37 °C. Cells were rinsed with PBS 3 times, pelleted, and resuspended in 1:1 DPBS/Matrigel (Corning). 5-week-old NOD SCID Gamma (NSG) female mice were obtained from Jackson Laboratories. Hair was removed from mice to ensure accurate orthotopic injection into the second mammary fat pad. Mice were briefly anesthetized using isoflurane to immobilize for the injection of 1 million tumor cells in 100 µL. For the bilateral studies, E-cad positive cell lines were implanted on the right side of the mouse and E-cad negative cell lines were implanted on the left side of the mouse ($N = 5$ for MDA-MB-231 study and $N = 10$ for MDA-MB-468 and MCF7 studies) and paired T.Test was used to calculate P-values (assume 2 tails for distribution).

For the inhibitor studies. MDA-MB-231+E-cad primary tumors were established in the second mammary fat pad on the left side of 5-week-old NSG female mice ($N = 5$ per group). Prior to start of treatment, all tumors were measured and animals were randomized to ensure comparable average starting tumor size per group. The MEK1/2 inhibitor PD0325901 (Selleckchem) was orally administered via peanut butter pellets daily for 5 days starting on day 8 post tumor cell injection at a dosage of 20 mg/kg and ending on day 12. Control group was given vehicle control (DMSO) in peanut butter pellet. All data are mean ± SEM. P-values determined Mann–Whitney test, two sided.

For both studies. Tumors were measured in two dimensions (x and y) with calipers every 3 days and weights of animals were recorded. Tumors were categorized as spheres or ellipses by calculating the difference between x and y. If $x-y < 1$mm, the tumor volume was calculated using the volume formula for a sphere. If $x-y > 1$mm, the tumor volume was calculated using the volume formula for an ellipse. At conclusion of the studies, mice were sacrificed using isoflurane and cervical dislocation. For bilateral tumor study, tumors were excised, weighed, and preserved for future studies. For inhibitor study, lungs and livers were also excised and preserved for future studies. All IHC staining was performed by an internal core facility.

For the tail vein "forced metastasis" model. Five-week-old female NSG mice were placed under heat lamp for 5–7 min to dilate tail veins ($N = 5$ per group) 100 µL of either E-cad+ or E-cad− cell solution (5000 cells/µL) was injected into the lateral tail vein using a 26-gauge needle. Mice were

monitored every three days and sacrificed 4 weeks post injection using isoflurane and cervical dislocation. Lungs were harvested and then inflated with 1.5% agarose prior to formalin fixation.

For all studies mentioned above, a priori power analysis was performed using t-tests in G*power 3.1.9.2 software using the following parameters: alpha as 0.05, power of 0.80, allocation ratio (N2/N1) as 1, effect size (d) are large, and analysis with two-tailed t-tests. No blinding was done in these studies.

Processing and analysis of harvested mouse tissues

Portions of primary tumors, lungs and liver were snap frozen in liquid nitrogen in addition to sections that were fixed in formalin were sent for sectioning and staining. H&E slides were obtained to visualize the tumor microenvironment or subjected to immunohistochemistry staining to assess protein expression in tissues. Protein was extracted from the primary tumor samples using 2× SDS sample buffer. Tumor tissue was broken down using tissue grinder, samples were then heated at 100 °C and sonicated. DNA was extracted from tumor tissue using DNA all prep kit (Qiagen).

Proteomics sample preparation

Sample preparation for proteomic and phosphoproteomic characterization were carried out as previously described [53, 54]. In brief, tumors were excised from the MDA-MB-231 bilateral study and immediately snap frozen in liquid nitrogen to ensure maximum preservation of phosphorylated proteins. Frozen tumor tissue ($N = 4$) was cryopulverized and resuspended in lysis buffer (8 M urea, 75 mM NaCl, 50 mM Tris-HCl, pH 8.0, 1 mM EDTA, 2 µg/mL aprotinin, 10 µg/mL leupeptin, 1 mM PMSF, 10 mM NaF, Phosphatase Inhibitor Cocktail 2 and Phosphatase Inhibitor Cocktail 3 (1:100 dilution), and 20 µM PUGNAc). To remove any particulates, lysates were centrifuged at $20,000 \times g$ for 10 min at 4 °C. Protein lysates were subjected to reduction with 5 mM, 1,4-Dithiothreitol for 30 min at room temperature. Then were subjected to alkylation with 10mM iodoacetamide for 45 min at room temperature, away from light. 50 mM Tris-HCl (pH 8.0) was used to reduce urea concentration to <2M. Samples were subjected to digestion of Lys-C (Wako Chemicals) (1:50) for 2 h at RT and then to trypsin (Promega) (1:50) overnight at room temperature. Generated peptides were then acidified to final concentration of 1% formic acid, subjected to clean-up using C-18 SepPak columns (Waters), and then dried utilizing a SpeedVac (ThermoScientific). Desalted peptides were then labeled with 10-plex Tandem-mass-tag (TMT) reagents following manufacturer's instructions (ThermoScientific). The samples were then reconstituted in volume of 20 mM ammonium formate (pH 10) and 2% acetonitrile (ACN) and subjected to basic reverse-phase chromatography with Solvent A (2% ACN, 5 mM ammonium formate, pH 10) and non-linear gradient of Solvent B (90% ACN, 5mN ammonium formatem pH 10) at 1 mL/min in the following sequence: 0% Solvent B for 9 min, 6% solvent B for 4 min, 6% increase to 28.5% solvent B over 50 min, 28% increase to 34% solvent B over 5.5 min, 34% increase to 60% solvent B over 13 min, ending with hold at 60% solvent B for 8.5 min – conducted on Agilent 4.6 mm × 250 mm RP Zorbax 300 A Extend-C-18 column with 3.5 µm beads (Agilent). Collected fractions were concatenated and 5% of fractions were alqiuopted for global proteomic analysis. Samples for global proteomic analysis were then dried down and resuspended in 3% ACN and 0.1% formic acid before ESI-LC-MS/MS analysis. The remaining 95% of sample was utilized for phosphopeptide enrichment and further concatenated using immobilized metal affinity chromatrography (IMAC). Ni-NTA agarose beads were used to prepare Fe^{3+}-NTA agarose beads, and then 300 µg of peptides reconstituted in 80% ACN/0.1% trifluoroacetic acid was incubated with 10 µL of Fe^{3+}-IMAC beads for 30 min. Samples were then centrifuged and supernatant was removed. Beads were washed 2× and then loaded onto equilibrated C-18 Stage Tips with 80% ACN, 0.1% trifluoroacetic acid. Tips were rinsed 2× with 1% formic acid. Sample was then eluted [3×] off the Fe^{3+}-IMAC beads and onto C-18 Stage tips with 70 µL of 500 mM dibasic potassium phosphate (pH 7.0). C-18 Stage Tips were washed 2x with 1% formic acid, followed by elution [2x] of phosphopeptides from C-18 stage tips with 50% ACN and 0.1% formic acid.

Following elution, samples were dried and resuspended in 3% ACN, 0.1% formic acid prior to ESI-LC-MS/MS analysis. One micrograms of peptide was separated using Easy nLC 1200 UHPLC system on an in-house packed 20 cm × 75 µm diameter C-18 column (1.9 µm Reprosil-Pur C-18-AQ beads (Dr. Maisch GmbH); Picofrit 10 µm opening (New Objective).

Column parameters: 50 °C, 0.300 μL/min with 0.1% formic acid, 2% acetonitrile in water and 0.1% formic acid, 90% acetonitrile. Using a 6–30% gradient over 84 min peptides were separated and analyzed using Thermo Fusion Lumos mass spectrometer (ThermoScientific). Following parameters were used- MS1: 60,000 for resolution, 350–1800 m/z for mass range, 30% for RF Lens, $4.0e^5$ for AGC Target, 50 ms for Max IT, 2–6 for charge state include, 45 s for dynamic exclusion, top 20 ions selected for MS2. For MS2: 50,000 for resolution, 37 for high-energy collision dissociation activation energy (HCD), 0.7 for isolation width (m/z), $2.0e^5$ for AGC Target, and 105 ms for Max-IT.

Proteomics data analysis

All LC–MS/MS files were analyzed by MS-PyCloud, a cloud-based proteomic pipeline developed at Johns Hopkins University. MS-PyCloud was used to perform database search for spectrum assignments, using MS-GF+ against a combined human and mouse UniprotKB Swiss-Prot database [55–57]. We focused on human-derived proteins for downstream analyses. False discovery rate at PSM, peptide, and protein levels were obtained using a decoy database [58]. Peptides were searched with two trypic ends, allowing for up to two missed cleavages. The following search parameters were used: 20 ppm precursor tolerance and 0.06 Da fragment ion tolerance, static modification of carbamidomethylation at cysteine (+57.02146), TMT-labeled modification of N-terminus and lysine (+229.1629) and variable modifications of oxidation of methionine (+15.99491), phosphorylation at serine, threonine, tyrosine (+79.96633). The following filters were used for global data analysis: one PSM per peptide, two peptides per protein, 1% FDR at protein level. The following filters were used for phosphoproteome data: one PSM per peptide, one peptide per protein, 1% FDR threshold at peptide level. Phosphopeptide-level data was used to examine overall relationship between substrates and kinases. Kinase-substrate associations were extracted from PhosphoSitePlus to eliminate phosphopeptides containing phosphosites that were not reported as well as those without associated kinases identified in our global dataset [59]. We then calculated the fold changed ($\log_2$ scale) and then ranked each tumor (greater than 1.5-fold increase) [53, 54].

Generation of heatmaps and volcano plots for proteomics data

Normalized $\log_2$ transformed protein expression values were used to generate heatmaps. Unsupervised hierarchical clustering was used to group samples (top dendrogram) and proteins (side dendrogram) using Euclidean distances. Heatmaps were generated in R, using the pheatmap package [60]. Normalized $\log_2$ transformed protein expression values were used to generate volcano plots. $\log_2$ fold changes were calculated between groups of samples. A two-tailed t-test was used to generate P-values. P-values were adjusted via a Benjamini-Hochberg procedure to correct for multiple comparisons. Statistically significant differential expression was determined to be greater than 1.5-fold change and an adjusted P-value < 0.05. Volcano plots were generated in R using the EnhancedVolcano package [61].

Proximity ligation assay

MDA-MB-231 E-cad− and E-cad+ cells were plated in 96-well glass bottom dish at 5000 cells/well. Wells were coated with collagen (50 μg/mL) prior to seeding the cells. After overnight incubation, cells were fixed using 4% PFA for 20 min at room temperature. MDA-MB-231 E-cad− cells were stained with EGFR (Rb) and E-cad (Ms) antibodies (full info in Table 6). MDA-MB-231 E-cad+ cells were stained with: EGFR (Rb) and E-cad (Ms), just EGFR (Rb), just E-cad (Ms), and with no antibodies. Duolink proximity ligation assay (Millipore-Sigma) was used to determine if EGFR and E-cad were interacting in MDA-MB-231 E-cad+ cells. After completion of the assay, wells were stained with phalloidin (f-actin) for 15 min at room temperature. Wells were then washed and DuoLink inSitu Mounting medium with DAPI (Millipore Sigma) was added to the wells. Confocal images were captured using a 40× oil objective and Nikon A1 Confocal microscope. The puncta in the images is first detected and counted used the previously developed particle tracking algorithm [62]. The cell and nuclei masks of individual cells were then obtained from the DAPI and phalloidin images based on the previously established segmentation algorithm[12] and the cell masks was then used to determine the number of puncta per cell. $N = 2$, $n = 2$–4. All data are mean ± SEM. P-values determined Mann–Whitney test, two sided.

Generation of tunable E-cadherin-zsGreen expressing cell lines

A DNA plasmid encoding the chemically tunable form of E-cadherin-zsGreen was stably transfected into MDA-MB-231 triple negative breast cancer cells as previously described [43].

Ex ovo chick embryo chorioallantoic membrane (CAM) platform

Fertilized white leghorn eggs were used to generate ex ovo chick embryos for extravasation efficiency assays and experimental metastasis assays [38, 41, 63]. In summary, freshly fertilized eggs (day 0) were incubated in a Sportsman Rocker Incubator at 37 °C and a relative humidity >45% for 4 days. Egg contents were removed from the eggshell as described in and placed into individual weigh boats on Day 4 [38, 64]. Each ex ovo embryo was returned to the incubator until Day 9 of embryonic development.

Experimental metastasis assay in the CAM of chick embryos

Each cell line was harvested and diluted into D-PBS (Gibco) at a concentration of 2×10^5 cells/mL. Using day 9 chick embryos, 2×10^4 cells (100 μL delivery volume) were intravenously (IV) injected into a small microvessel (20 μm diameter) to minimize bleeding post-IV injection. Equal distribution of cancer cells arrested throughout the CAM was confirmed using a fluorescence stereoscope (Nikon). Injected CAMs were returned to the incubator. At Day 18, each CAM was enumerated for the number of metastases (single metastasis ≥ 5 cells/colony) using a fluorescence stereoscope. For the MDA-MB-231 cell line expressing the E-cadherin-zsGreen-DD protein (chemically tunable E-cadherin with Shield-1 ligand), 50 μL of Shield-1 (5 μM, 5% EtOH in D-PBS, Takeda Inc.) was I.V. injected into each embryo on days 12, 14, and 16 as described by Leong et al. [43].

Extravasation efficiency assay in the CAM of chick embryos

Each cell line was harvested and diluted into D-PBS (Gibco) at a concentration of 1×10^6 cells/mL. Using Day 13 chick embryos, 1×10^5 cells (100 μL delivery volume) were IV injected into a small microvessel (20 μm diameter) to minimize bleeding post IV injection. At $t = 0$ after IV injection of cancer cells, individual cancer cells within a 1.5×1.5 cm field of view (as described in Leong et al.) were enumerated using a fluorescence stereomicroscope and then returned to an incubator [38]. At $t = 24$ h post IV injection, l*ens culinaris* agglutinin-Rhodamine (Vector Laboratories Inc.) was IV injected (20 μg/embryo) to visualize the CAM microvasculature and vessel lumen. After agglutinin injection, the same field of view on each embryo was enumerated for extravasated cancer cells using an upright confocal microscope (Fast A1R, Nikon). Only cells that had extravasated past the CAM, i.e., not overlapping with rhodamine signal, were enumerated.

TCGA analysis for correlation with *CDH1* (E-cad) expression

TCGA analysis for CDH1 expression with GSEA gene sets was performed as described previously [65]. Briefly, RNA-seq V2 data for basal breast cancer tumors from the Pan-Cancer Atlas initiative of The Cancer Genome Atlas (TCGA) were used for analyses. Gene set statistics were computed with hallmark and curated gene sets from MSigDB and CDH1 expression using a one-sided Wilcoxon gene set test in LIMMA. Gene sets with FDR adjusted P-values below 0.05 were considered significantly enriched.

Statistical analysis

Figure legends and above sections describe statistical tests used for individual experiments with P-values in figure captions. Variance was assessed for all groups prior to running statistical tests.

DATA AVAILABILITY

REFERENCES

1. van Roy F, Berx G. The cell-cell adhesion molecule E-cadherin. Cell Mol Life Sci. 2008;65:3756–88.

2. Polyak K, Weinberg RA. Transitions between epithelial and mesenchymal states: acquisition of malignant and stem cell traits. Nat Rev Cancer. 2009;9:265–73.

3. Thiery JP, Acloque H, Huang RYJ, Nieto MA. Epithelial-Mesenchymal Transitions in Development and Disease. Cell. 2009;139:871–90.

4. Hartsock A, Nelson WJ. Adherens and tight junctions: Structure, function and connections to the actin cytoskeleton. Biochim Biophys Acta Biomembr. 2008;1778:660–9.

5. Bajpai S, Correia J, Feng Y, Figueiredo J, Sun SX, Longmore GD, et al. Catenin mediates initial E-cadherin-dependent cell-cell recognition and subsequent bond strengthening. PNAS. 2008;105:18331–6.

6. Li CI, Anderson BO, Daling JR, More RE. Trends in incidence rates of invasive lobular and ductal breast carcinoma. J Am Med Assoc. 2003;289:1421–4.

7. Liu JB, Feng CY, Deng M, Ge DF, Liu DC, Mi JQ, et al. E-cadherin expression phenotypes associated with molecular subtypes in invasive non-lobular breast cancer: evidence from a retrospective study and meta-analysis. World J Surg Oncol. 2017;15:139.

8. Padmanaban V, Krol I, Suhail Y, Szczerba BM, Aceto N, Bader JS, et al. E-cadherin is required for metastasis in multiple models of breast cancer. Nature. 2019;573:439–44.

9. Chu K, Boley KM, Moraes R, Barsky SH, Robertson FM. The paradox of E-cadherin: role in response to hypoxia in the tumor microenvironment and regulation of energy metabolism. Oncotarget. 2013;4:446–62.

10. Rodriguez FJ, Lewis-Tuffin LJ, Anastasiadis PZ. E-cadherin's dark side: possible role in tumor progression. Biochim Biophys Acta Rev Cancer. 2012;1826:23–31.

11. Curtis C, Shah SP, Chin SF, Turashvili G, Rueda OM, Dunning MJ, et al. The genomic and transcriptomic architecture of 2,000 breast tumours reveals novel subgroups. Nature 2012;486:346–52.

12. Na TY, Schecterson L, Mendonsa AM, Gumbiner BM. The functional activity of E-cadherin controls tumor cell metastasis at multiple steps. Proc Natl Acad Sci USA. 2020;117:5931–7.

13. Cavallaro U, Christofori G. Cell adhesion and signalling by cadherins and Ig-CAMs in cancer. Nat Rev Cancer. 2004;4:118–32.

14. Pece S, Gutkind JS. Signaling from E-cadharins to the MAPK pathway by the recruitment and activation of epidermal growth factor receptors upon cell-cell contact formation. J Biol Chem. 2000;275:41227–33.

15. Kovacs EM, Ali RG, McCormack AJ, Yap AS. E-cadherin homophilic ligation directly signals through Rac and phosphatidylinositol 3-kinase to regulate adhesive contacts. J Biol Chem. 2002;277:6708–18.

16. Zantek N, Azimi M, Fedor-Chaiken M, Wang B, Brackenbury R, Kinch M. E-cadherin regulates the function of the EphA2 receptor tyrosine kinase. Cell Growth Differ. 1999;10:629–38.

17. Fedor-Chaiken M, Hein PW, Stewart JC, Brackenbury R, Kinch MS. E-cadherin binding modulates EGF receptor activation. Cell Communication and Adhes. 2003;10:105–18.

18. Ramírez Moreno M, Bulgakova NA. The Cross-Talk Between EGFR and E-Cadherin. Front Cell Dev Biol. 2022;9:828673

19. Alpaugh ML, Tomlinson JS, Shao ZM, Barsky SH. A novel human xenograft model of inflammatory breast cancer. Cancer Res. 1999;59. http://aacrjournals.org/cancerres/article-pdf/59/20/5079/2472940/5079.pdf.

20. Patil PU, D'Ambrosio J, Inge LJ, Mason RW, Rajasekaran AK. Carcinoma cells induce lumen filling and EMT in epithelial cells through soluble E-cadherin-mediated activation of EGFR. J Cell Sci. 2015;128:4366–79.

21. Stockinger A, Eger A, Wolf J, Beug H, Foisner R. E-cadherin regulates cell growth by modulating proliferation-dependent β-catenin transcriptional activity. J Cell Biol. 2001;154:1185–96.

22. Soler C, Grangeasse C, Baggetto LG, Damour O. Dermal fibroblast proliferation is improved by β-catenin overexpression and inhibited by E-cadherin expression. FEBS Lett. 1999;442:178–82.

23. Heibeck TH, Ding SJ, Opresko LK, Zhao R, Schepmoes AA, Yang F, et al. An extensive survey of tyrosine phosphorylation revealing new sites in human mammary epithelial cells. J Proteome Res. 2009;8:3852–61.

24. Lee MH, Russo GC, Rahmanto YS, Du W, Crawford AJ, Wu PH, et al. Multi-compartment tumor organoids. Mater Today. 2022;61:104–16.

25. Crawford AJ, Forjaz A, Bhorkar I, Roy T, Schell D, Queiroga V, et al. Precision-engineered biomimetics: the human fallopian tube. bioRxiv. 2023. https://doi.org/10.1101/2023.06.06.543923.

26. Dai X, Cheng H, Bai Z, Li J. Breast cancer cell line classification and Its relevance with breast tumor subtyping. J Cancer. 2017;8:3131–41.

27. Liu K, Newbury PA, Glicksberg BS, Zeng WZD, Paithankar S, Andrechek ER, et al. Evaluating cell lines as models for metastatic breast cancer through integrative analysis of genomic data. Nat Commun. 2019;10:2138.

28. Wu PH, Gilkes DM, Phillip JM, Narkar A, Cheng TWT, Marchand J, et al. Single-cell morphology encodes metastatic potential. Sci Adv. 2020;6:eaaw6938.

29. Sonnaert M, Papantoniou I, Luyten FP, Schrooten J. Quantitative validation of the Presto Blue^TM metabolic assay for online monitoring of cell proliferation in a 3D perfusion bioreactor system. Tissue Eng Part C Methods. 2015;21:519–29.

30. Dhillon AS, Hagan S, Rath O, Kolch W. MAP kinase signalling pathways in cancer. Oncogene. 2007;26:3279–90.

31. Polakis P. Wnt signaling in cancer. Cold Spring Harb Perspect Biol. 2012;4:9.

32. Barrett SD, Bridges AJ, Dudley DT, Saltiel AR, Fergus JH, Flamme CM, et al. The discovery of the benzhydroxamate MEK inhibitors CI-1040 and PD 0325901. Bioorg Med Chem Lett. 2008;18:6501–4.

33. Ravi D, Bhalla S, Gartenhaus RB, Crombie J, Kandela I, Sharma J, et al. The novel organic arsenical darinaparsin induces MAPK-mediated and SHP1-dependent cell death in T-cell lymphoma and hodgkin lymphoma cells and human xenograft models. Clin Cancer Res. 2014;20:6023–33.

34. Wright CJM, McCormack PL. Trametinib: first global approval. Drugs 2013;73:1245–54.

35. Paulo JA, Mcallister FE, Everley RA, Beausoleil SA, Banks AS, Gygi SP. Effects of MEK inhibitors GSK1120212 and PD0325901 in vivo using 10-plex quantitative proteomics and phosphoproteomics. Proteomics 2015;15:462–73.

36. Bajpai S, Feng Y, Wirtz D, Longmore GD. β-Catenin serves as a clutch between low and high intercellular E-cadherin bond strengths. Biophys J. 2013;105:2289–300.

37. Iorns E, Drews-Elger K, Ward TM, Dean S, Clarke J, Berry D, et al. A new mouse model for the study of human breast cancer metastasis. PLoS ONE. 2012;7:e47995.

38. Kim Y, Williams KC, Gavin CT, Jardine E, Chambers AF, Leong HS. Quantification of cancer cell extravasation in vivo. Nat Protoc. 2016;11:937–48.

39. Chaturvedi P, Gilkes DM, Wong CCL, Kshitiz, Luo W, Zhang H, et al. Hypoxia-inducible factor-dependent breast cancer-mesenchymal stem cell bidirectional signaling promotes metastasis. J Clin Investig. 2013;123:189–205.

40. Romero-Fernandez W, Carvajal-Tapia C, Prusky A, Katdare KA, Wang E, Shostak A, et al. Detection, visualization and quantification of protein complexes in human Alzheimer's disease brains using proximity ligation assay. Sci Rep. 2023;13:11948.

41. Leong HS, Robertson AE, Stoletov K, Leith SJ, Chin CA, Chien AE, et al. Invado-podia are required for cancer cell extravasation and are a therapeutic target for metastasis. Cell Rep. 2014;8:1558–70.

42. Williams KC, Cepeda MA, Javed S, Searle K, Parkins KM, Makela AV, et al. Inva-dodopodia are chemosensing protrusions that guide cancer cell extravasation to promote brain tropism in metastasis. Oncogene. 2019;38:3598–615.

43. Leong HS, Lizardo MM, Ablack A, McPherson VA, Wandless TJ, Chambers AF, et al. Imaging the impact of chemically inducible proteins on cellular dynamics in vivo. PLoS ONE. 2012;7:e30177.

44. Fantozzi A, Christofori G. Mouse models of breast cancer metastasis. Breast Cancer Res. 2006;8:212.

45. MEK Inhibitor PD-325901 To Treat Advanced Non-Small Cell Lung Cancer. Iden-tifier NCT00174369. Pfizer, 2005-2007. https://clinicaltrials.gov/study/NCT00174369 (accessed 2023).

46. Henderson YC, Chen Y, Frederick MJ, Lai SY, Clayman GL. MEK inhibitor PD0325901 significantly reduces the growth of papillary thyroid carcinoma cells in vitro and in vivo. Mol Cancer Ther. 2010;9:1968–76.

47. Haura EB, Ricart AD, Larson TG, Stella PJ, Bazhenova L, Miller VA, et al. A phase II study of PD-0325901, an oral MEK inhibitor, in previously treated patients with advanced non-small cell lung cancer. Clin Cancer Res. 2010;16:2450–7.

48. Brown AP, Carlson TCG, Loi CM, Graziano MJ. Pharmacodynamic and tox-icokinetic evaluation of the novel MEK inhibitor, PD0325901, in the rat following oral and intravenous administration. Cancer Chemother Pharmacol. 2007;59:671–9.

49. Lee MH, Wu PH, Staunton JR, Ros R, Longmore GD, Wirtz D. Mismatch in mechanical and adhesive properties induces pulsating cancer cell migration in epithelial monolayer. Biophys J. 2012;102:2731–41. https://doi.org/10.1016/j.bpj.2012.05.005.

50. Giri A, Bajpai S, Trenton N, Jayatilaka H, Longmore GD, Wirtz D. The Arp2/3 complex mediates multigeneration dendritic protrusions for efficient 3-dimensional cancer cell migration. FASEB J. 2013;27:4089–99.

51. Wu PH, Gilkes DM, Phillip JM, Narkar A, Wen-Tao Cheng T, Marchand J, et al. Single-cell morphology encodes metastatic potential. 2020. https://www.science.org

52. Fraley SI, Wu PH, He L, Feng Y, Krisnamurthy R, Longmore GD, et al. Three-dimensional matrix fiber alignment modulates cell migration and MT1-MMP utility by spatially and temporally directing protrusions. Sci Rep. 2015;5:14580.

53. Clark DJ, Dhanasekaran SM, Petralia F, Pan J, Song X, Hu Y, et al. Integrated proteogenomic characterization of clear cell renal cell carcinoma. Cell. 2019;179:964–983.e31.

54. Mertins P, Tang LC, Krug K, Clark DJ, Gritsenko MA, Chen L, et al. Reproducible workflow for multiplexed deep-scale proteome and phosphoproteome analysis

of tumor tissues by liquid chromatography-mass spectrometry. Nat Protoc. 2018;13:1632–61.

55. Chen L, Zhang B, Schnaubelt M, Shah P, Aiyetan P, Chan D, et al. MS-PyCloud: an open-source, cloud computing-based pipeline for LC-MS/MS data analysis. bioRxiv. https://doi.org/10.1101/320887.

56. Kim S, Pevzner PA. MS-GF+ makes progress towards a universal database search tool for proteomics. Nat Commun. 2014;5:5277.

57. Kim S, Gupta N, Pevzner PA. Spectral probabilities and generating functions of tandem mass spectra: a strike against decoy databases. J Proteome Res. 2008;7:3354–63.

58. Elias JE, Gygi SP. Target-decoy search strategy for increased confidence in large-scale protein identifications by mass spectrometry. Nat Methods. 2007;4:207–14.

59. Hornbeck PV, Zhang B, Murray B, Kornhauser JM, Latham V, Skrzypek E. PhosphoSitePlus, 2014: Mutations, PTMs and recalibrations. Nucleic Acids Res. 2015;43:D512–20.

60. Kolde, R. Package 'pheatmap'. CRAN. 2022; 1.0.12.

61. Blighe K, Rana S, Lewis M. EnhancedVolcano: Publication-ready volcano plots with enhanced colouring and labeling. Bioconductor. 2018; 1.20.0.

62. Wu PH, Hale CM, Chen WC, Lee JSH, Tseng Y, Wirtz D. High-throughput ballistic injection nanorheology to measure cell mechanics. Nat Protoc. 2012;7:155–70.

63. Leong HS, Chambers AF, Lewis JD. Assessing cancer cell migration and metastatic growth in vivo in the chick embryo using fluorescence intravital imaging. In: Hoffman RM, editor. In vivo cellular imaging using fluorescent proteins: methods and protocols. Totowa, NJ: Humana Press; 2012. p. 1–14. https://doi.org/10.1007/978-1-61779-797-2_1.

64. Debord LC, Pathak RR, Villaneuva M, Liu HC, Harrington DA, Yu W, et al. The chick chorioallantoic membrane (CAM) as a versatile patient-derived xenograft (PDX) platform for precision medicine and preclinical research. Am J Cancer Res. 2018;8. www.ajcr.us/ISSN:2156-6976/ajcr0080963.

65. Nair PR, Danilova L, Gómez-De-Mariscal E, Kim D, Fan R, Muñoz-Barrutia A, et al. MLL1 regulates cytokine-driven cell migration and metastasis. bioRxiv. 2022. https://doi.org/10.1101/2022.10.18.512715.

ACKNOWLEDGEMENTS

AUTHOR CONTRIBUTIONS

GCR and DW developed the hypothesis and designed experiments. GCR performed most experiments and data analysis. AJC, JC, RC, MNK, BS, and MHL assisted with the experiments. VWR assisted with proximity ligation assay. DC, TL, HZ performed proteomics experiments, assisted in the analysis, and edited the manuscript. BS and HSL performed CAM experiments, assisted in the analysis, and edited the manuscript. QZ assisted with the Metabric analysis of clinical data. PRN analyzed TCGA invasive breast carcinoma data sets for correlation with E-cad (CDH1) expression. PW assisted with image analysis. GCR and DW wrote the manuscript with input from AJC and VWR.

COMPETING INTERESTS

The authors declare no competing interests.

ADDITIONAL INFORMATION

Supplementary information The online version contains supplementary material available at https://doi.org/10.1038/s41388-024-03007-2.

Correspondence and requests for materials should be addressed to Denis Wirtz.

Reprints and permission information is available at http://www.nature.com/reprints

Publisher's note Springer Nature remains neutral with regard to jurisdictional claims in published maps and institutional affiliations.